Bulletin of Physics Projects 1, 2016, 10-13

Bulletin of Physics Projects

Journal homepage: http://www.bbcphysics.in/journal.html

Study of Thunderstorm over NER of India from Kalpana 1 Satellite TIR images

Deva Prasad Majumdar and Diganta Kumar Sarma[#]

Department of Physics, B. Borooah College, Ulubari, Guwahati-781007, Assam, India

[#]E-mail address: sarma.diganta@gmail.com

Abstract

This work deals with the study of thunderstorm over the north eastern region of india with the help of thermal infra-red data from Kalpana 1 satellite. For that purpose data from 15th April to 28th May 2010 are considered. Frequency of occurrence of thunderstorm is observed to be more in the month of May compared to April. The duration of thunderstorm follows a lognormal distribution. Thunderstorm of duration 2 hours has maximum number of occurrences. Number of occurrences of thunderstorms is observed to be maximum between 4-8 UTC i.e. between 09:30 to 14:30 IST.

1. Introduction

Thunderstorm is a severe weather phenomenon characterized by the presence of lightning and thunder and usually accompanied by heavy rainfall, hail or no precipitation at all. Thunderstorms result from the rapid upward movement of warm, moist air initiated by unequal warming of Earth's surface. Lifting of this air results in condensation and release of latent heat and thus cumulonimbus cloud is formed which can reach heights up to 20 km [1]. When the rising air reaches its dew point, water droplets and ice particles are formed and start falling a long distance through the clouds towards Earth's surface and become larger by colliding with other droplets. These falling droplets create a downdraft air that spreads out the Earth's surface causing strong winds associated with thunderstorms. Thunderstorm can be as small as few km in diameter to as big as few 100km diameter with time span of less than one hour to several hours. Thunderstorms are primarily of four types:

- Single cell
- Multi-cell cluster
- Multi-cell lines
- Super-cell

(i) *Single cell:* Single cell refers to a single thunderstorm with one main updraft. Such storms are rarely severe and are a result of local atmospheric instability and hence termed as 'air mass thunderstorm'. Single thunderstorm last normally 20-30 min.

(ii) *Multi-cell cluster*: Multi-cell storms form as clusters of storms where each line may last only 20 min but the cluster itself may present for hours at a time. They often arise from convective updrafts in or near mountain ranges and linear weather boundaries usually strong cold fronts or troughs of low pressure. These types of storms are stronger than single cell but much weaker than super-cell storm. Hazards with such storms include moderate sized hail, flash flood and weak tornadoes.

(iii) Muli-cell lines: cumulonimbus clouds are often arranged in long lines, 150km to 200 km in length in which adjacent clouds are very close to each other. This

mesoscale convective system accompanied by a line of squalls ahead of it is referred to as multicell lines.

(iv) supercell: storms with wind shear, separate downdrafts and updrafts and a long rotating updraft are called as super-cell thunderstorms. These are the most powerful type of thunderstorms having such powerful updrafts that can break through the troposphere and reach into lower levels of the stratosphere. Super-cell thunderstorm produces destructive tornadoes, extremely large hailstones, strong winds and flash flood.

All thunderstorms, regardless of its type, undergo through three stages-

- Developing stage
- Mature stage
- Dissipation stage

Developing stage: In this stage, parcels of warm humid air rise and condense to form cumulus clouds releasing large amount of latent heat. Hence, the inside of the cloud remains warmer than the surrounding air. The clouds continue to develop as long as more humid air added to it from bellow. The updraft air forms a low pressure zone beneath the forming thunderstorm [2].

Mature stage: during this stage, the warm humid air continues to rise until it reaches existing air which is warmer and the air can rise no further. The water droplets coalesce into larger droplets and freeze to become ice particles and while falling they melts into rain. However at times the updraft is strong enough to held aloft long enough to be so large that they do not melt completely and fall as hail. Falling rain creates downdraft though updraft is present and this simultaneous presence of both updraft and downdraft marks the mature stage of a thunderstorm producing cumulonimbus clouds. In this stage, considerable internal turbulences can occur in the storm system causing strong wind, severe lightning and tornadoes.

Dissipating stage: in this stage, the thunderstorm is dominated by the downdraft. If the atmospheric conditions do not support super-cellular development, this stage occurs rather quickly approximately within 20-30 min from the development of the thunderstorm begins. The cool air carried to the ground by the downdraft cuts off the inflow of the thunderstorm, the updraft disappears and the thunderstorm dissipates.

Thunderstorms can develop in any geographic location. During the pre-monsoon season of April and May, north-east India gets severe thunderstorms [3]. Severe thunderstorms create lot of hazards to population and landscape through the strong wind, large hail and occasional tornadoes accompanying them. A large number of field experiments had been conducted towards thunderstorms in various parts of India. With the help of remote sensing technology such as Doppler weather radar, satellite technology etc. Department of science and technology, Govt. of India conducted a national coordinate programme on "Severe Thunderstorm Observation and Regional Modeling (STORM) during the time frame 2007-2009. The objectives of this study are:

(i) Observation of thunderstorm from the IR data obtained from Kalpana 1 satellite.

(ii) To find the frequency and duration of thunderstorm affecting North-East India for 2010.

(iii) Occurrence of thunderstorm during different time domain of a day.

(iv) Comparison of occurrence of thunderstorm within North Eastern Region (NER) and outside NER.

(v) To study the developing & decay, duration and severity of a thunderstorm as case study over NER.

2. System description and data analysis:

For the present study, hourly satellite image in Thermal Infrared and water vapour channel from Kalpana-1 satellite for two months of April and May 2010, were taken. The data are being provided by North Eastern Space Application Center (NESAC) which is a center of Department of space located at Shillong.

METSAT (renamed as Kalpana - 1on February 5, 2003 after the Indian born American Astronaut Dr. Kalpana Chawla, who died on February 1, 2003 in the US Space Shuttle Columbia disaster) is the first in the series of exclusive meteorological satellites built by ISRO. The specifications of the satellite are listed in Table 1.

A brief description on Thermal Infra-Red (TIR) images are given bellow-

Thermal Infra Red (IR) Images: The Earth's surface and the cloud over it emits radiation continuously (with peak at TIR band having wavelength in the range 10-12μm) which is a function of the temperature of the emitting body. TIR image is generated by receiving these emitted radiations from the Earth's surface and cloud over it. However, since the emitted radiation must traverse the Earth's atmosphere before reaching the satellite, it is modified during passage by atmospheric absorption and re-emission. Thermal Infra Red images show the temperature of the land, the sea or the tops of the clouds above them. Decrease in temperature implies higher and denser cloud while higher temperature indicates land or sea without cover. The conventional displaying of IR images is black and white to represent the clouds in white shades against the darker background of the Earth. Since the temperature decreases normally with height, the IR radiation with the lowest intensity is emitted by the highest and coldest clouds and these appear as whitest. IR images

are available 24 hours per day as temperatures can be measured, regardless of day and night. The temperatures can be represented in a grey scale or in a color scheme

Table 1: Specifications of METSAT

Mission	Meteorological
Spacecraft Mass	1060 kg mass (at Lift-off) 498 kg (Dry mass)
Onboard Power	550 Watt
Payload	Very High Resolution Radiometer (VHRR) Data Relay Transponder (DRT)
Launch Date	12 September 2002
Launch Site	SHAR, Sriharikota
Launch Vehicle	PSLV-C4
Orbit	Geostationary (74° East Longitude)
Mission	7 Years

Storm looks like a big swirling mass of clouds in any of the image spectrums whether it may be IR. The brighter white the clouds appear, the denser and higher into the cloud tops are. Strong storms are characterized by penetrating high into the atmosphere and by displaying obvious signs of rotation.

3. Results and Discussions

3.1. Frequency and duration of Thunderstorm over NER)

The TIR data collected from NESAC for the period of 15th April to 28th May 2010 are studied to find out the frequency and duration of thunderstorm occurred in NER. Figure 1 shows the number of occurrences of thunderstorm for each day. It can be observed from the Fig. 1 that occurrence thunderstorm is more in the month of May compared to April.

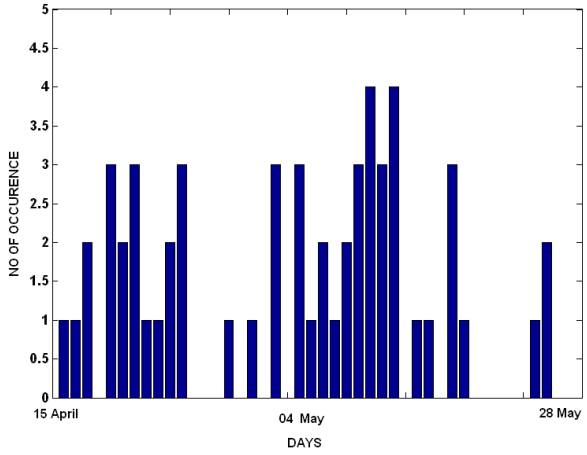

Figure 1: Number of occurrence of thunderstorm for the period 15th April to 28th May 2010.

Duration of the thunderstorm for the same days is also estimated. Figure 2 shows the number of occurrence of thunderstorm of different time duration. Form the figure 2 it can be inferred that thunderstorm of duration two hours are maximum in number. Thunderstorms with higher duration are less in number. It is very interesting to observe that the duration of thunderstorm nearly follows a lognormal distribution.

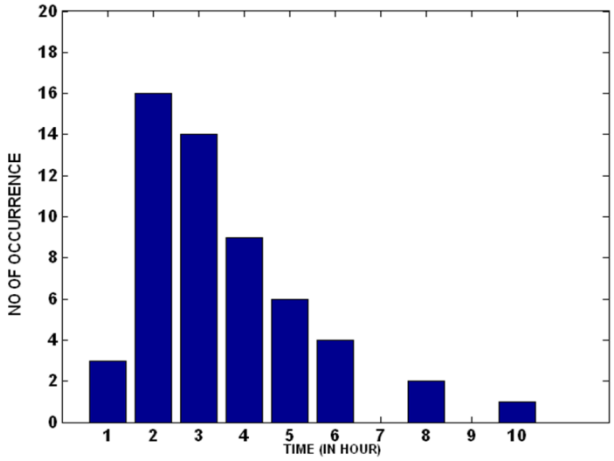

Figure 2: Duration of thunderstorm for the period 15th April to 28th May 2010

3.2. Occurrence of TS for different time Domain

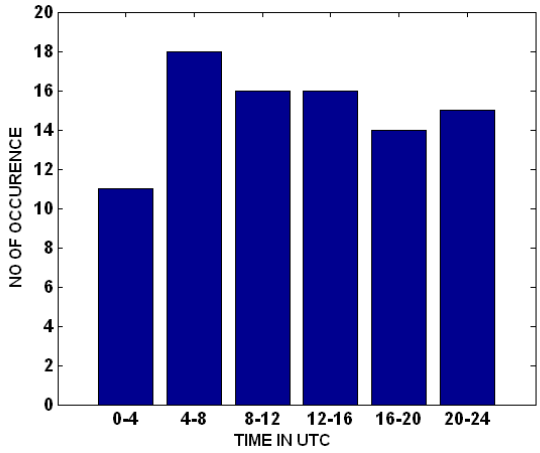

Figure 3: Number of occurrence of TS within different time domain.

From the one and half month data collected we have studied the number of occurrences of thunderstorms for six time domain viz. 0-4 UTC, 4-8 UTC, 8-12 UTC, 12-16 UTC, 16-20, UTC and 20-24 UTC. Figure 3 shows the number of occurrences of thunderstorms for the said time domain. It can be inferred from the figure that the occurrence of thunderstorm, for the months of April and May is maximum for the time domain of 4-8 UTC i.e. 09:30 to 13:30 IST.

3.3. Developing and decay of a thunderstorm

Out of the two months data a thunderstorm event on 11th and 12th May 2010 is considered here to study how it developed and decayed. From the IR images as observed

by Kalpana-1 satellite the thunderstorm starts developing at 1400 UTC on 11th May 2010 near Dhubri (Figure 4). Then in the subsequent time it grows up and covers nearly whole of lower Assam. It starts decaying after 0300 UTC on 12th May.

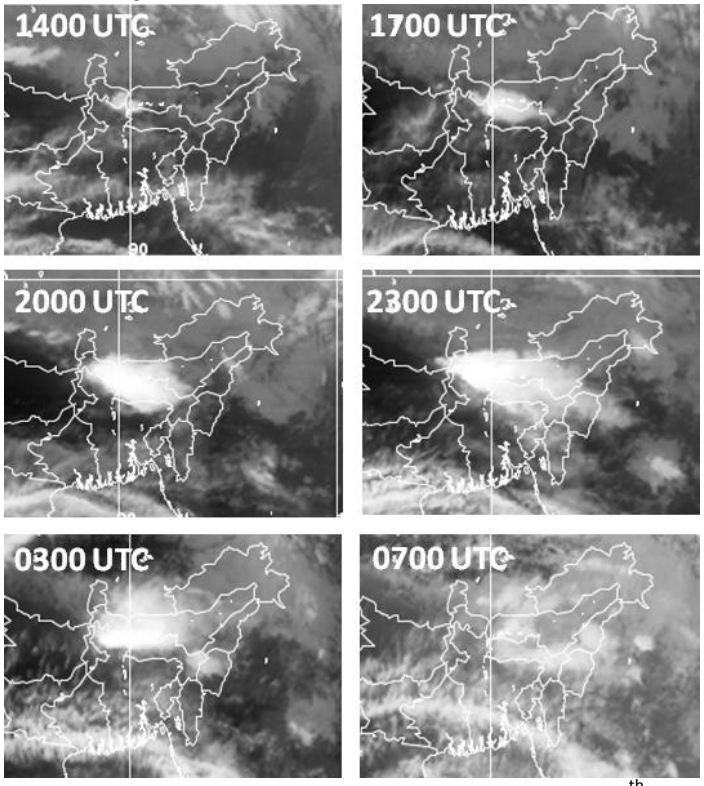

Figure 4: Developing and decay of thunderstorm on 11th and 12th May 2010

4. Conclusions

This observation has been conducted on various aspects of thunderstorm over North Eastern Region of India. The TIR data given by Kalpana-1 Geostationary satellite is collected from NESAC, Shillong. One and half month data on April and May 2010 is utilized for the present study.

The main conclusions of this study are:

(i)Thunderstorms can be studied with the help of TIR data from Kalpana-1 satellite.

(ii) Frequency of thunderstorm is observed to be more in the month of May than April.

(iii) The duration of thunderstorm follows a lognormal distribution. Thunderstorm of duration 2 hours has maximum number of occurrences.

(iv) Number of occurrences of thunderstorms is observed to be maximum between 4-8 UTC i.e. between 09:30 to 14:30 IST.

5. Acknowledgement

The authors would like to thank the Director, NESAC for allowing visit to the station and using the Satellite data. Authors would like to acknowledge Dr. Arup Borgohain and Mr. Shyam sundar Kundu from NESAC for their valuable suggestions and help during the work.

6. References

[1] Chris C. Mooney (2007). Storm world: hurricanes, politics, and the battle over global warmin. Houghton Mifflin Harcourt. p. 20. ISBN 9780151012879

[2] Gianfranco Vidali (2009). "Rough Values of Various Processes". University of Syracuse. Retrieved 2009-08-31

[3] G. K. Manohar, S. S. Kandalgaonkar , M. I. R. Tinmaker, Thunderstorm activity over India and the Indian southwest monsoon, J. Geophysical Res., Vol. 104, No. D4, PP. 4169-4188, 1999

Bulletin of Physics Projects 1, 2016, 14-19

Bulletin of Physics Projects

Journal homepage: http://www.bbcphysics.in/journal.html

Plasma Parameter Measurement with a Langmuir Probe in a Weakly Ionized Plasma

Ibnul Farid, Shivajyoti Sarma and Homeswar Kakati[#]

Department of Physics, B. Borooah College, Ulubari, Guwahati-7, Assam, India

[#]Email: kakatidr@gmail.com

Abstract

The present work is aimed at studying the plasma production technique by hot cathode filament discharge method, Langmuir probe diagnostic technique to calculate different plasma parameters e.g. plasma density (n_e), electron temperature (T_e), plasma potential (V_P) etc. and to find out the variation of the above mentioned plasma parameters with discharge current (I_d). Plasma parameters define various characteristics of plasma. Factors like plasma density (n_e), electron temperature (T_e), plasma potential (V_P) has a great significant impact on study of plasma. It is observed in our project that plasma density is 5-10 x 10^{15} m^{-3} and electron temperature is 2.4 - 3 eV. It is also observed that the plasma density increases linearly with the discharge current due to the increase of primary electrons which ionizes the neutral gas atoms.

1. Introduction

Plasma is a distinct phase of matter, separate from the traditional solids, liquids, and gases. It is a collection of charged particles that respond strongly and collectively to electromagnetic fields, taking the form of gas - like clouds or ion beams. Since particles in plasma are electrically charged, it is frequently described as an "ionized gas".

The term "Plasma" was first used by American physicist Irving Langmuir and Tonks in 1923 to describe the ionized gas. By definition, plasma is a *quasineutral* gas of charged and neutral particles which exhibits *collective behavior*. *Quasineutral* means, the number density of positive ions and electrons are nearly equal, $n_e \approx n_i$ and by the term *collective behaviour* means the motions that depend not only on local conditions but also on the state of plasma in remote region as well. In plasma, particles experience Columbic force which is a long range force in nature and becomes weaker at very large distance. On the other hand, in neutral gases the force between two particles is governed by the Van der-Walls' force which is a short range force. Almost 99% of the matter in the universe e.g., the Sun, stars, nebula, the Milky Way etc. are in plasma state. Plasma phenomena near our earth are rare due to its low temperature and density. One can produce plasma on earth only by experimental means. In our everyday lives we encounters with plasmas are limited to a few examples: the flash of a lightning bolt, the soft glow of the Aurora Borealis, the conducting gas inside a fluorescent tube or neon sign and the slight amount of ionization in a rocket exhaust.

In order to convert a gas into plasma state, it is very necessary to tear away at least some of the electrons from the atoms. By these we convert the atoms into ions. This de-attachment of electrons from atom is called "ionization". In the laboratory, ionization can be produced by various methods. The most important of these are (a*) ionization by electric discharge* (b) *ionization by heat* (c) *ionization by radiation.*

The most widely used method in laboratory for obtaining plasma is the electrical gas discharge method. When we apply electric field to a gas in the double plasma device in between two charged conductors i.e. one positively charged and one negatively charged, it is necessary that the electric field applied to the gas is large enough so that energy imparted to the electrons is sufficient to knock out at least one electron from an atom on impact. These primary electrons, after accelerated by the applied electric field will collide with the neutral particles and will generate new free charge carries. In this way, electrons multiplication proceeds. Thus ionization of an entire gas occurs and turns into plasma.

All substance became ionized if they are heated sufficiently to a very high temperature. This process is known as "thermal ionization". It is necessary that the temperature be close to the energy of the most weakly bound electron i.e. almost equal to the lowest ionization energy of an atom or molecule. In atom the valance electron is in the outer orbit. By heating, we de-attach the electron and ionize the gas. Thus we obtain thermal plasma in laboratory. The radiation emitted by the sun, hot stars causes ionization in the surrounding gases, vapors and interstellar gas and in this way also plasma gets produced. In order to sustain plasma in a gas, the conditions are: $\lambda_D \ll L$, $N_D \gg 1$, $\omega\tau > 1$, where, λ_D is the Debye length, L is dimension of chamber, N_D is number of particles in a Debye sphere, ω is frequency of oscillation and τ is mean time between two collisions of charged particles with neutral atom.

The basic parameters of plasma are-

a) The particle density n which is measured in particle *per cubic meter*.
b) The temperature T of each species which is usually measured in *electron volt (eV).*
c) The steady state magnetic field B which is measured in *Tesla.*

Other subsidiary plasma parameters *e.g.* Debye length, Lamoure radius, plasma frequency, cyclotron frequency *etc*. can be derived from the above mentioned three plasma parameters.

3. Experimental

3.1. Description of the experimental set-up

Figure 1 shows the photograph of the existing double plasma device in Centre of Plasma Physics- Institute for Plasma Research (CPP-IPR), Sonapur, Assam. The cylindrical shaped chamber, made of stainless steel (SS 304L), is 1.2 *m* long and 0.3 *m* in diameter. The chamber is connected to a vacuum unit consisting of a diffusion pump backed by a rotary pump. Penning and Pirani gauges are connected in the pumping lines to measure the diffusion and rotary pump created pressure readings respectively.

Fig. 1: Photograph of the existing double plasma device in Centre of Plasma Physics - Institute for Plasma Research (CPP-IPR), Sonapur, Assam.

This diffusion-rotary pump combination reduces the pressure inside the chamber up to 7×10^{-6} *millibar*. In order to confine the charged particles, two cylindrical shaped multi-dipole magnetic cages, each of having length 0.32 *m* and diameter 0.25 *m* are inserted inside the chamber. These two magnetic cages are made up of fourteen vacuum sealed rectangular channels, which contain small square sized strontium ferrite magnets. Both these magnetic cages are insulated from each other as well as from the inner wall of the plasma chamber by some ceramic insulators. Two SS channels containing similar type of strontium ferrite magnets that have been used in the multi-dipole magnetic cages are inserted in between these cages to form the N-S pole of a transverse magnetic field**.** This type of a double plasma setup with a transverse magnetic filter field between the source and target regions is called as a '*tandem*' source.

3.2. Plasma production technique

Initially, the pressure inside the chamber is reduced up to 7×10^{-6} *millibar* by the diffusion-rotary pump combination and then the pressure is raised to the range of 10^{-4} *millibar* by injecting hydrogen gas. Plasma can be produced in any one of the magnetic cages by filament discharge method. The magnetic cage where plasma is produced is called as 'Source' or 'Driver' cage. The cage to which plasma diffuses after production in the source magnetic cage is called the 'Target' or 'Extraction' cage.

Plasma is produced in the source magnetic cage by hot cathode filament discharge method. In this method, initially the filament (usually of Tungsten) is heated sufficiently by passing current to emit electrons. These electrons are called primary electrons. Simultaneously the filament (cathode) is biased negatively with respect to the source magnetic cage (anode) and the latter is connected to ground. The primary electrons after emitting from the surface of the filament gain energy due to their acceleration towards the source magnetic cage and on their way they will suffer successive collisions with the neutral hydrogen gas molecules and atoms. If the electron energy is sufficiently high compared to the ionization energy of the hydrogen gas atom, then ionization occurs and thus plasma is produced inside the chamber. After production in the source cage, plasma diffusion takes place to the target magnetic cage through the transverse magnetic field.

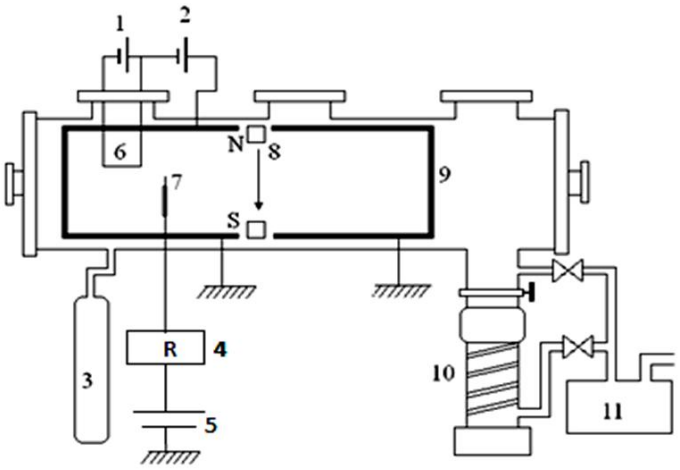

Fig. 2: Schematic diagram of the experimental set up. The different parts labeled are (1) Filament voltage power supply (V_F), (2) Discharge voltage power supply (V_D), (3) Hydrogen gas cylinder, (4) Resistance, (5) Power supply, (6) Tungsten filament, (7) Cylindrical Langmuir probe, (8) Transverse magnetic field (N- North Pole, S- South pole), (9) Multi-dipole magnetic cage, (10) Diffusion pump, (11) Rotary pump.

3.3. Langmuir probe

Langmuir probe is the simplest and most frequently used tool for measuring different plasma parameters *e.g.* plasma density (n_e), electron temperature (T_e), plasma potential (V_p), floating potential (V_f), electron distribution function *etc*. Irving Langmuir (1881-1957) first developed this technique about fifty years ago. A Langmuir probe is basically a metal conductor which is inserted into plasma and electrically biased with respect to any reference electrode to collect electron or ion current. From this *I-V* characteristic one can easily calculate different plasma parameters. Figure 3.3 shows an ideal Langmuir probe characteristic.

An ideal Langmuir probe characteristic can be divided into three parts *viz. ion saturation region* (*A*), *transition region* (*B*) and *electron saturation region* (*C*). When the probe is at the same potential (V_P) with its surrounding plasma (V_S), the existing electric field between the probe and plasma vanishes immediately. In this situation, the electrons whose mobility is higher due to their lower mass compared to the ions strikes the probe. Therefore, the current collected by the probe is predominantly electron current. Now, if the probe is biased positively with respect to the plasma potential (V_S), the electrons are accelerated whereas the ions are repelled by the probe.

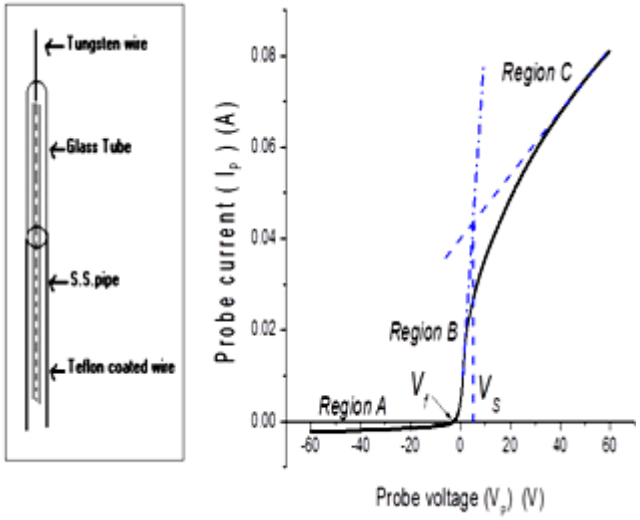

Fig. 3: I-V Characteristics of Langmuir Probe

For a sufficiently high positive probe potential the ion current to the probe vanishes and a space charge layer of electrons build up near the surface of the probe. Because of this space charge layer the electron current to the probe saturates. When the probe potential is negative with respect to the plasma potential, the probe repels the electrons and accelerates the ions. Now, if the electron distribution is Maxwellian, the shape of the probe current curve in the transition region would be exponential. At a certain probe potential, the ion and electron flux to the probe becomes same. This potential is called the *floating potential* (V_f). At a large value of negative probe potential, a space charge layer of positive ions develops and the probe collects only the positive ions.

When the probe voltage V_P is sufficiently negative with respect to the plasma potential V_S, the probe collects the ion saturation current (I_{is}). For a Maxwellian ion distribution at temperature T_i, the dependence of the ion current I_i (V_P) on V_P is given by-

$$I_i(V_p) = -I_{is} \exp\left(\frac{e(V_s - V_p)}{kT_i}\right) \text{ when } V_p \geq V_s \ldots (1)$$

$$I_i(V_p) = -I_{is}, \text{ when } V_p < V_s \ldots\ldots\ldots\ldots\ldots\ldots (2)$$

When $T_e > T_i$, the ion saturation current can be written as-

$$I_{is} = 0.6 \times e \times n_e \times A_p \times \left(\frac{kT_e}{m_i}\right)^{1/2} \quad \ldots\ldots\ldots (3)$$

where, e is elementary charge, n_e is electron density, A_P is the probe surface area, T_e is the electron temperature, k is Boltzmann's constant and m_i is the mass of the atom (H atom in our case).

For $V_P >> V_S$, the probe collects electron saturation current I_{es}. The electron current as a function of V_P can be expressed as-

$$I_e(V_p) = -I_{es} \exp\left(\frac{e(V_s - V_p)}{kT_i}\right) \text{ when } V_p \leq V_s \ldots (4)$$

$$I_e(V_p) = I_{es} \text{ when } V_p > V_s \ldots\ldots\ldots\ldots\ldots\ldots\ldots (5)$$

The electron saturation current I_{es} is given by:

$$I_{es} = \frac{1}{4} e n_e \nu_{e,th} A_p \ldots\ldots\ldots\ldots\ldots\ldots\ldots\ldots (6)$$

where, $\nu_{e,th} = \sqrt{\frac{8kT_e}{\pi m_e}}$ is the average velocity of the electron

Now taking the semi log of equation (4), we get-

$$\ln I_e(V_p) = -\frac{e(V_s - V_p)}{kT_e} + \ln I_{es} \ldots\ldots\ldots\ldots\ldots (7)$$

$$\text{or, } \ln I_e(V_p) = \frac{eV}{kT_e} + \ln I_{es} \ldots\ldots\ldots\ldots\ldots\ldots (8)$$

where, $V = (V_P - V_S)$ equation is straight line. If $\ln I_P(V_P)$ is plotted against V, equation will give a straight line with a slope equal to e/kT_e which gives a good measure of electron temperature.

For the present project, at first voltage applied to the filament and the filament voltage and current are kept constant at 7V and 12A. The discharge voltage and current are fixed at 80 V and 0.5 A. The Langmuir probe, which is in the source region, is biased from -80 V to +80 V to obtain the I-V characteristics. After that the discharge current is varied from 0.5 A to 2 A by changing the filament voltage and in each time the Langmuir probe I-V characteristics are obtained.

4. Results and discussion

The density of the neutral hydrogen atom is $n_a = P/kT_g$, where T_g is the temperature of the neutral gas; P is the neutral gas pressure, k is Boltzmann const. For P = 5x10^{-4} mbar and T_g= 300 K, n_a = 1.2077x10^{19} m^{-3}. For I_d = 1.5 A, we get n_i = 9.016x10^{15} m^{-3}. We obtain n_i/n_a= 7.465x10^{-4} . Thus only .074% of the neutral atoms are ionized. From our calculation we have found that the plasma inside the chamber is weakly ionized.

Figure 4 shows the I-V characteristics of Langmuir probe for 0.5 A discharge current . For collision mean free paths, $\lambda = \frac{1}{n_a \sigma}$ where σ is the cross-section area of collision and its value for H is 0.88x10^{-20} m^2. So λ = 9.40 m. Thus the relativity long mean free path explains the relatively low value of the ionization percentage i.e. electrons that are energetically capable of ionizing atoms are more likely to make it to the wall before ionizing an atom. Since, mean free path > chamber dimension so the plasma is *collision less*.

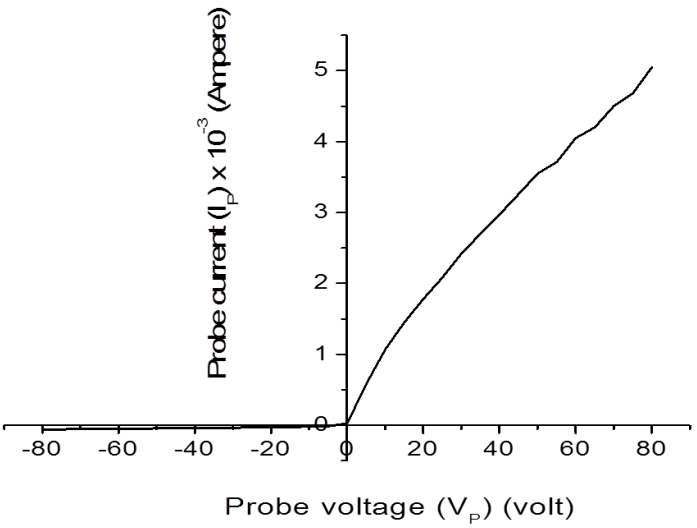

Fig. 4: I-V Characteristics

Figure 5 shows the plot of $\ln I_P$ vs. V_P. The electron temperature can be calculated from the slope of the straight line which is drawn in the transition region of the probe characteristics. It is found that the electron temperature for 0.5 A discharge current is ~ 2.5 eV

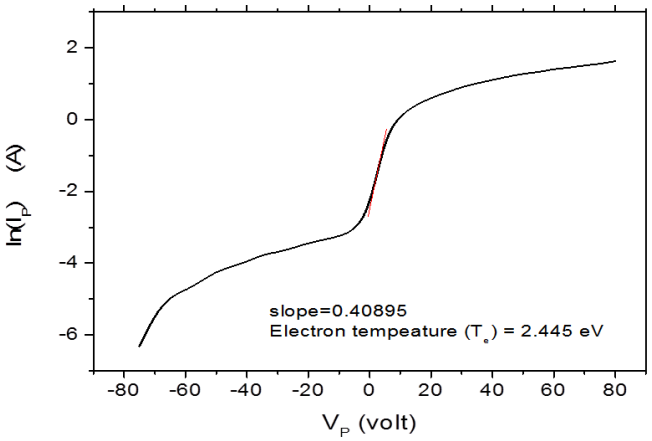

Fig. 5: ln I_p vs. V_p curve

4.1. Variation of plasma parameters with discharge current

To verify the plasma parameter variation with discharge current, the discharge current is varied from 0.5 A to 2 A and the discharge voltage kept constant at 80 V as shown in the Fig. 6. Figure 7 shows the variation of

plasma density with respect to the discharge current. The plasma density linearly increases with respect to the discharge current. In our experiment the discharge current is increased by increasing the filament current. As the filament current increases the thermionic emission from the filament also increases. The electrons emitted from the filament are called the primary electrons and their energy is equivalent to eV_d. So, for 80 V discharge current, the primary electron energy would be around 80 eV. And the number density of this electron is a function of filament voltage. These primary electrons are responsible for the ionization of the background neutral gas and as their number density increases with discharge current, more ionization occurs. Therefore, the plasma density increases with respect to the discharge current.

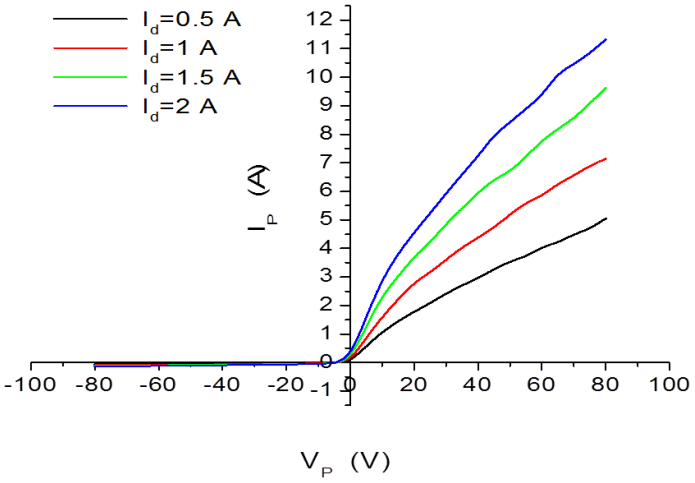

Fig. 6: I-V characteristics of Langmuir probe for I_d= 0.5 A, 1 A, 1.5 A and 2 A

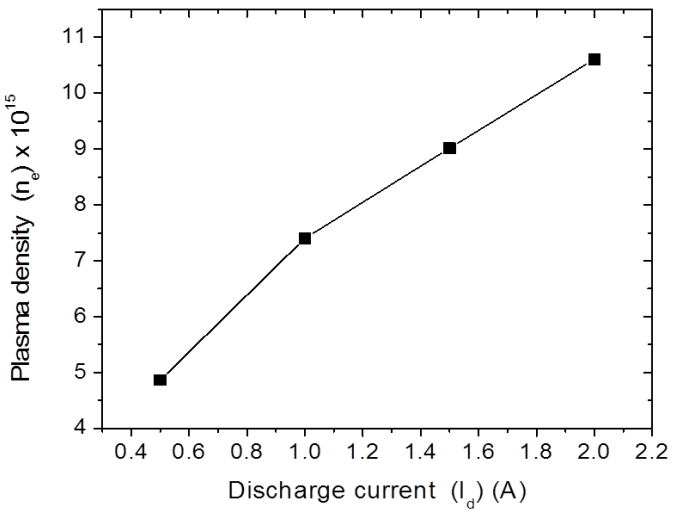

Fig. 7: Variation of plasma density with respect to the discharge current

Figure 8 shows the variation of electron temperature with respect to the discharge current and it is observed that like plasma density, the electron temperature also increases as we increase the discharge current. As the discharge current increases the number of primary electrons emitted from the filament also increases and these primary electrons increase the average energy of the plasma.

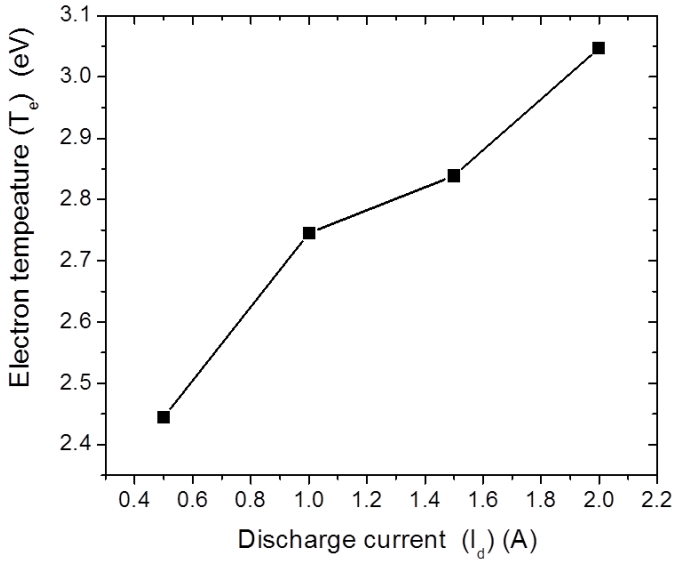

Fig. 8: Variation of electron temperature with respect to the discharge current

5. Conclusion:

From the above study, we have observed that the hot filament discharge technique is an efficient method for the production of cold plasma. The plasma density and electron temperature are calculated from the I-V characteristics of Langmuir probe and we have obtained these as $5-10\times10^{15}\,m^{-3}$ and 2.4 - 3 eV. We have also observed that the plasma density increases linearly with the discharge current due to the increase of primary electrons that ionizes the neutral gas atoms. Because of these primary electrons the average temperature of the electrons inside the chamber also goes up.

6. Acknowledgement

We would like to express our sincere gratitude to Dr. M. Chakraborty for his guidance. We are also thankful to Ph.D. scholars Mr. B.K. Das and Miss P. Hazarika for their constant help and support. We would like to thank Dr. K.S. Goswami, director of CPP-IPR, for providing us with the facilities necessary to carry out our project. .

7. References

[1] L. Tonks and I. Langmuir, Phys. Rev. **34**, (1929), p. 876.

[2] F. F. Chen, *'Introduction to plasma physics and controlled fusion'*, second edition Vol 1, Springer. (2009) (second Indian reprint)

[3] Robert L. Merlin o, Am. J. Phys, 75(12), December 2007, p.1078

[4] A. M. Howatson, *'An introduction to gas discharges'*, Pergamon press, second edition, (1976).

[5] D. A. Frank-Kamenetskii, *'Plasma the fourth state of matter'*, Planum press, (1972).

[6] B. K. Das. Ph. D thesis submitted in Gauhati University. 'A study of plasma dynamics across a magnetic filter field in a double plasma device', (2014).

Bulletin of Physics Projects 1, 2016, 20-23

Bulletin of Physics Projects

Journal homepage: http://www.bbcphysics.in/journal.html

A comprehensive study of Rydberg's constant with reference to different elements

Partha P. Goswami, Chinmoy J. Rajbongshi, Jishnukesh Das, Hirak Jyoti Kalita, Nilufar Yashmin Prodhani, Akhil Chandra Das*

Department of Physics, B. Borooah College, Ulubari, Guwahati-7, Assam, India

*Email address: akhilchdas@gmail.com

Abstract

This work is aimed at the determination of the Rydberg's constant for various elements. We have selected Hydrogen, Helium, Neon, Sodium and Mercury for the purpose. From the study using apparatus available in undergraduate level laboratory we found that the value of Rydberg's constant for various elements are almost same though it should vary with the nuclear mass of the element.

1. Introduction:

Spectroscopy as a field of experimental and theoretical research has contributed to our knowledge not only about our own Earth but of the Sun, of interstellar space and the distant stars. Experimental determination of Rydberg's constant put Bohr's theory into verification. Theoretical value of Rydberg's constant for any element is:

$$R_{element} = \frac{m_r e^4}{8c\epsilon_0^2 h^3} \quad \text{.....(1)}$$

where, m_r is the reduced mass of the electron and nucleus system of the element, e =1.6×10^{-19} C, charge of the electron, c = 3X10^8 ms^{-1}, velocity of light in vacuum ϵ_0=8.854×10^{-12} farad m^{-1}, permittivity of free space n = 1, 2, 3, 4.....quantum numbers related with different orbits h = 6.62×10^{-32} Js, Planck constant. If the experimental value of Rydberg's constant is found to be well within the range of theoretical value consistency and success of Bohr's theory of atom, basically the Hydrogen atom may be confirmed.

The history of the study of the distinct colors obtained in the analysis of radiation emitted from an excited gas in discharge tube, called spectral lines, dates back to the late 19th century, when a high school mathematics teacher from Basel, Switzerland, named Johann Balmer put forward an empirical rela*tion describing the wavelengths of the visible spectra of H_2 gas. However, he could not support his relation with suitable physical explanation. In a paper written in 1885, Balmer proposed that his relation could be used to predict the entire spectrum of Hydrogen, including the ultraviolet and infrared ranges. He showed that, within the limits of experimental error, wavelength of each line of a series is given by the simple relation:

$$\lambda = B\frac{n_2^2}{n_2^2 - n_1^2} \quad \text{.....(2)}$$

where B=3645.6 A^0 and n_1 and n_2 are small integers. The best arrangement for the visible series was obtained by putting n_1 =2 throughout and n_2 =3, 4, 5, 6 … for the first, second, third, fourth..… member of the series. Almost at the same time Rydberg was in search of a general relation for all series and put forward the following relation in terms of wave number:

$$\overline{\upsilon_n} = \overline{\upsilon_\infty} - \frac{R}{(n+\mu)^2} \quad \text{.....(3)}$$

where $\overline{\upsilon_n}$ is the wave number of n[th] line of the spectrum and $\overline{\upsilon_\infty}$, μ and R are constants. The constant R is now known as Rydberg's constant after Rydberg's name. Since n takes integral values only, the visible series of Hydrogen affords a direct means of calculating this constant R.

The announcement by Bohr in the year 1913 of his theory for hydrogen atoms marks the beginning of a new era in spectroscopy and atomic structure. On the basis of three fundamental assumptions Bohr gave the expression for total energy of the electron in different stationary orbits of the Hydrogen atom to be:

$$E_n = -\frac{me^4Z^2}{8\epsilon_0^2 n^2 h^2} \quad \ldots\ldots(3)$$

and wavelength of the emitted radiation to be:

$$\frac{1}{\lambda} = \frac{me^4Z^2}{8\epsilon_0^2 h^3}\left(\frac{1}{n_f^2} - \frac{1}{n_i^2}\right)$$

$$\frac{1}{\lambda} = RZ^2\left(\frac{1}{n_f^2} - \frac{1}{n_i^2}\right) \quad \ldots\ldots(4)$$

where, $R = \frac{me^4}{8c\epsilon_0^2 h^3}$ =109737.424 cm^{-1}which is called the Rydberg constant.

In deriving the above relation, mass of the nucleus is supposed to be infinite in comparison to mass of the electron. From classical mechanics it can be shown that reduced mass of the electron and nucleus system of an element is:

$$m_r = \frac{m}{1+\frac{m}{M}} \quad \ldots\ldots(5)$$

where, M is the mass of nucleus. Thus, Rydberg's constant for infinite mass of nucleus can be written as:

$$R_\infty = R = \frac{me^4}{8c\epsilon_0^2 h^3} = 109737.424 \text{ cm}^{-1} \quad \ldots\ldots(6)$$

When the effect of finite mass is taken into account 'm' must be replaced by 'm_r' and the expression for Rydberg's constant becomes-

$$R_{element} = \frac{m_r e^4}{8c\epsilon_0^2 h^3} = \frac{me^4}{8c\epsilon_0^2 h^3\left(1+\frac{m}{M}\right)}$$

$$R_{element} = \frac{R_\infty}{\left(1+\frac{m}{M}\right)} \quad \ldots\ldots(7)$$

Thus, for Hydrogen:

$$R_H = \frac{R_\infty}{\left(1+\frac{m}{M_H}\right)}$$

Hence, for Hydrogen, under the condition, finite mass of nucleus, equation (4) can be written as:

$$\frac{1}{\lambda} = R_H\left(\frac{1}{n_f^2} - \frac{1}{n_i^2}\right) \quad \ldots\ldots(8)$$

Equations (1), (2), (6) are equivalent which can be used for the study of spectra of different elements. They can be generalized in form of Rydberg's relation:

$$\frac{1}{\lambda_n} = \overline{\upsilon_n} = \frac{R}{(n_f+\mu_f)^2} - \frac{R}{(n_i+\mu_i)^2} \quad \ldots\ldots(9)$$

where, the factor (n+μ) is called Rydberg's denominator.

According to Bohr's theory of circular orbits as well as Sommerfeld's theory of elliptical orbits of Hydrogen, there is no difference in energy between two orbits with same total quantum number 'n'. In complex atoms, on the other hand, there is considerable energy difference between the levels arising from s, p, d and f elements of the same total quantum number. This difference in energy is attributed to the various amounts of penetration of the different electron orbits into the electron sub-shells. Taking penetration into account and noting that the quantum number 'n' is in general greater than Rydberg's denominator (n+μ) Rydberg's relation (7) may be modified as follows

$$\frac{1}{\lambda_n} = \overline{\upsilon_n} = \frac{R}{(n_f-\mu_f)^2} - \frac{R}{(n_i-\mu_i)^2} \quad \ldots\ldots(10)$$

and spectral term value:

$$T = \frac{R}{(n-\mu)^2} = \frac{R}{n_{eff}^2} \quad \ldots\ldots(11)$$

Where n is now the total quantum number and the factor (n-μ) is called the Rydberg's denominator. μ is the quantum defect and n_{eff} is the so called effective quantum number. For atoms having larger values of atomic number z, mean distance of the outer most electrons from the nucleus increases and the electric field acting on the electron approaches to that acting on the electron of the Hydrogen atom. In other words, for larger value of n, the chances of penetration of electron into atomic trunk are less and value of quantum defect is also less for higher values of 'n' and l(s, p, d, f etc.).

Again from the theory diffraction grating if θ is the angle of diffraction of Nth order primary maximum then:

$$sin\theta = mN\lambda$$

where, m is the number of rulings per unit length of the grating and **λ** is the wavelength of light used . Hence:

$$m = \frac{sin\theta}{N\lambda} \quad \ldots\ldots(12)$$

and

$$\lambda = \frac{sin\theta}{mN} \quad \ldots\ldots(13)$$

Wavelengths λ_n and λ occurred in equations (8) and (10) are same, hence using them the following relation can be obtained:

$$\frac{mN}{sin\theta} = \frac{R}{(n_f-\mu_f)^2} - \frac{R}{(n_i-\mu_i)^2} \quad \ldots\ldots(14)$$

which can be used for determination of Rydberg's constant of different elements provided μ_f and μ_i are known [1].

3. Experimental set up:

In this experiment the wavelength of prominent color of different light sources are measured using a diffraction grating and a spectrometer. A diffraction grating with more number of rulings per mm and a good spectrometer with least count as small as possible have been used. The spectrometer is leveled with leveling screws and spirit

level. Width of the slit is adjusted to be very narrow. A sodium lamp is placed in front of the slit of the spectrometer and it is then adjusted for parallel rays by Schuster's method. Vernier constant of the Vernier scale attached to the spectrometer is noted down. The grating is placed at the middle of the prism table vertically so that it is perpendicular to the incident ray from the collimator and its unrulled surface facing the collimator of the spectrometer. Angles of diffraction of 1st and 2nd order are determined for sodium yellow line and number of rulings per unit length of the diffraction grating is determined using the known wavelength of sodium yellow light (5893 Å). The sodium discharge tube is replaced by Hydrogen discharge tube and angle of diffraction for different colours are determined. Same procedure is repeated for Helium, Neon, Sodium and Mercury. Rydberg's constant for different elements have been determined using equation (11) and available data of quantum defect for different transitions of different elements. Proportional error involved in determination of wavelength and Rydberg's constant have also been determined. Theoretical value of Rydberg's constant for experimental elements have been calculated using equation (5).

4. Results and Discussions:

Table 1 presents the experimentally obtained data for the determination of value of ruling per unit length of the diffraction grating employing a Sodium source of known wavelength 5893×10^{-8} cm.

The values of Rydberg's constant as determined for different elements are tabulated in Table 2. Experimental determination of Rydberg's constant put Bohr's theory into verification. Theoretical value of Rydberg's constant for any element is:

$$R_{element} = \frac{m_r e^4}{8c\epsilon_0^2 h^3}$$

Experimental values of Rydberg's constant are well within the range of theoretical values remembering the proportional error involved in measurement of wavelength of different spectral lines.

Table 1: Experimental values for rulings per cm of the gratings used for experiment

Order of diffraction	Angle of diffraction	Rulings per cm	Average rulings per cm
1st	21.0888	6100	6062
2nd	45.2313	6024	

This verifies the consistency and success of Bohr's theory of atom, basically the Hydrogen atom. For other many electron atoms Bohr's theory is applicable with modification. Bohr's atomic theory takes into account of the transitions where principal quantum numbers are involved but silent about the transition from s, p, d, f etc. sublevels of same principal quantum number. Hence, modified form of Rydberg's empirical formula is to be used to study Rydberg's constant for elements other than Hydrogen taking quantum defect into account due to penetration of orbits into atomic core. This type of experimental study may be used to study the quantum defect using the theoretical values of Rydberg's constant for different elements. Quantum defect for different elements for different energy levels (s, p, d, f etc.) are important.

Table 2: Determination of Rydberg's constant for different elements using diffraction grating

Source	Order of diffraction	Angle of diffraction (θ) (degrees)	sin θ	Experimental value of wavelength of the emission line (λ) (x 10^{-8} cm)		Value of Rydberg's constant (cm^{-1})	Average value of Rydberg's constant (cm^{-1})
Hydrogen	1st	23.58884	0.4001705	Red	6560.1	109754.42	110327.54
		17.13111	0.2945592	Green	4828.8	110558.31	
	2nd	52.15000	0.7896198	Red	6512.8	110669.90	
Helium	1st	23.85430	0.4044122	Red	6623.1	108710.40	107433.76
		17.33083	0.2978885	Green	4878.6	109320.90	
	2nd	56.96000	0.8382901	Red	6912.0	104233.37	
Neon	1st	23.84319	0.4042348	Red	6626.8	109237.45	115684.07
	2nd	45.98000	0.7190072	Red	5929.0	122130.70	
Sodium	1st	21.08880	0.3598144	Yellow	5898.5	109631.80	110072.22
	2nd	45.23000	0.7099395	Yellow	5853.0	110512.64	

Due to lack of accurate value of quantum defect for different elements, calculation of Rydberg's constant cannot be carried out correctly for some elements like Neon, Mercury etc. The percentage error for the experiment was found to be 1.715%. The average value of Rydberg's constant for the experimental elements was found to be 110879.3975 cm^{-1}. The average value of proportional error was obtained to be 0.01895

Thus, the final value of the Rydberg's constant obtained from the experiment is 110879.3975 ± 2101.1646 cm^{-1}.

5. Conclusions:

The value of Rydberg's constant obtained in the present work is found to be in good agreement with the actual theoretical value. The technique employed here is well suited to undergraduate level. The gratings required for this purpose must have large number of rulings per cm. Some discrepancies though might arise due to certain limitations in the experimental procedure. Discharge tube used in undergraduate level laboratories are defective in the sense that level of evacuation and filling appropriately with the particular element at appropriate pressure is not done. This may introduce inaccuracy in the determination of Rydberg's constant. Experimental determination of Rydberg's constant determining the wavelength of spectral lines requires very high precision spectrometers.

6. References

[1] Atomic Spectrs by G.E. White and other undergraduate level books on atomic physics.

Bulletin of Physics Projects, 1, 2016, 24-28

Bulletin of Physics Projects

Journal homepage: http://www.bbcphysics.in/journal.html

Study of Fraunhofer Diffraction Patterns for Different Slits and Measurement of Hair Diameter Using Diffraction Phenomena

Pritom Singh, Jayanta Das and S. Banerjee[#]

Department of Physics, B. Borooah College, Ulubari, Guwahati-7, Assam, India

[#] E-mail address: somikbnrj@gmail.com

Abstract

The present paper describes an arrangement for experimental observation and investigation of Fraunhofer diffraction patterns for different types of slits. The variation of dark fringe width as a function of the dark fringe number on both sides of the central maximum elucidates that the fringe width in case of diffraction is not constant and the dark fringe width increases non-linearly on both sides of the central maximum. This signifies that the bright fringe width decreases non-linearly on both sides of the central maximum and so does the intensity. The measurement of hair diameter using diffraction yielded values of 116.96 μm and 76.02 μm which are consistent with the average human hair diameter obtained from microscopic experiments.

1. Introduction

Diffraction of light is a phenomenon that provides evidence of the wave characteristics of Light. The deviation observed in the rectilinear propagation of light due to the presence of a slit or obstacle in its path is known as diffraction. Diffraction phenomena always occur when the free propagation of light is changed by obstacles such as iris diaphragm or slits [1]. Diffraction phenomena are generally classified into two major classes:

(i) Fresnel Class of diffraction and
(ii) Fraunhofer Class of diffraction

In case of Fresnel diffraction, the light source and the screen are at a finite distance from the diffraction object. With increasing distances Fresnel diffraction patterns are increasingly similar to Fraunhofer diffraction [1].

In case of Fraunhofer diffraction, parallel wave fronts are studied in front of the diffraction object and behind it. This corresponds to a light source which is at infinite distance from the diffraction object on one side and on the other side the screen too is at infinite distance from the object.

However, applying a Laser source it is much easier to obtain Fraunhofer diffraction patterns. The light waves emitted by Lasers have a plane wavefront [2]. Moreover, the beam spot size for Lasers is very small and there is minimum spreading as such lenses are not required for obtaining a diffraction pattern. Fraunhofer diffraction patterns are mathematically much easier to analyze as compared to Fresnel diffractions. This is the reason as to why we chose to investigate the Fraunhofer diffraction patterns formed by different types of slits/apertures. In the present paper, we present a comprehensive study of the experimentally observed Fraunhofer diffraction patterns formed by single slit, double slit and triangular slit using a He-Ne Laser source. The experimental variation of the dark fringe width for the single slit patterns were investigated and were theoretically validated. We have also demonstrated the use of diffraction phenomena to determine the diameter of human hair.

2. Experimental Details

The schematic diagram for the experimental set-up designed for the said experiment is shown in the Fig. 1. It consists of a He-Ne Laser set up at one end of an optical bench and a white screen on the other end.

The slits used for the experiments have to be mounted between the laser source and the screen on the optical bench in some upright mounts with the option of height adjustment and capable of being moved along the optical bench. It is evident from the Fig. 1, that we have not used any lenses for performing the experiment. This is because the wavefront of light emitted by a laser source is already a plane wavefront and as such the light seems to be coming from infinity and as such no lenses are required for observing diffraction patterns.

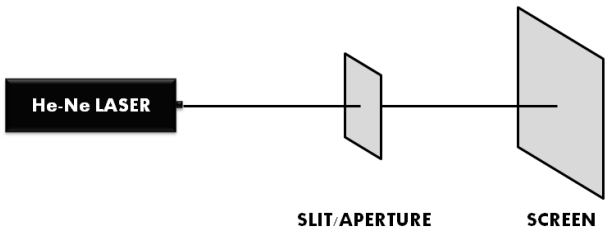

Fig. 1: Schematic diagram for the experimental arrangement to observe Fraunhofer diffraction patterns using He-Ne laser source.

The actual set-up is shown in the Fig. 2 with the students taking measurements of the fringe width. In the actual set-up, a vernier calipers having least count of 0.02 mm was attached to the screen such that the fringe width can be measured with accuracy.

Fig. 2: Students taking measurement using the actual experimental set-up.

In the present paper, we have studied the diffraction patterns obtained by three different types of slits: (a) single slit, (b) double slit and (c) triangular slit. These slits were designed using knife edges obtained from a blade by breaking it into two halves. These knife edges were arranged in the form of a single, double and triangular slits using cardboards and black tape.

The distance from the laser to the screed for the experimental set-up was fixed at 158.5 cm whereas the distance from the screen to the slit was 129.6 cm. The distance between the slit and the laser was obtained as (158.5 -129.6) cm = 28.9 cm. The wavelength of the He-Ne Laser source was 635 nm.

The same experimental set-up was also employed for the purpose of measurement of human hair diameter. The human hair was placed in lieu of the slit and the diffraction pattern obtained was investigated.

3. Results and Discussions

3.1. Diffraction patterns from different slits

Fig. 3(a-c) shows the diffraction patterns obtained from a He-Ne laser source by using a single, double and triangular slits, respectively.

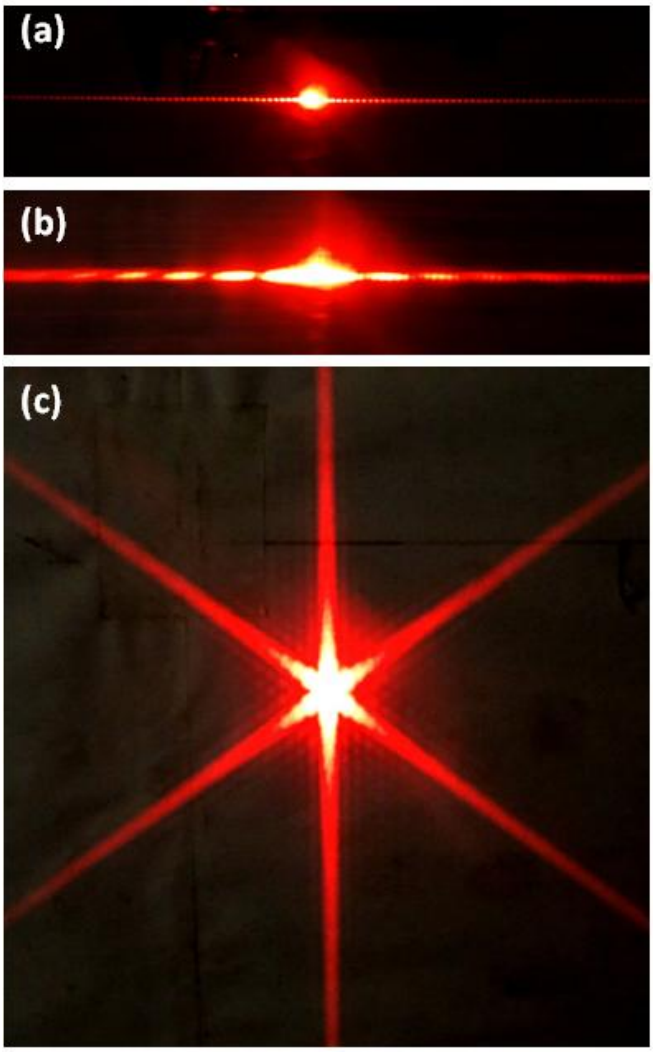

Fig. 3: Fraunhofer diffraction patterns for (a) single slit, (b) double slit and (c) triangular slits.

The variations of dark fringe width were studied as we move away from the central bright maxima in order to validate the experimental findings with the well established theory of Fraunhofer diffraction due to a single slit.

The detailed data collected has been tabulated below. Table 1 shows the variation of the dark fringe width as a function of the number of dark fringes towards the right of the central maximum.

On the other hand, Table 2 shows the variation of the dark fringe width for the dark fringes towards the left of the central maximum. The fringe widths have been measured using vernier calipers.

Table 1: Variation of dark fringe width as a function of the dark fringe number towards right of the central maximum

Fringe No.	Right side of central maximum			Left side of central maximum			Fringe Width $d = d_1 \sim d_2$ (cm)
	M.S.R. (cm)	V.S.R.	Total (d_1) (cm)	M.S.R. (cm)	V.S.R.	Total (d_2) (cm)	
1	6.2	13	6.226	6.1	37	6.174	0.052
2	5.8	25	5.850	5.7	47	5.792	0.058
3	5.5	2	5.504	5.4	21	5.442	0.062
4	5.1	9	5.118	5.0	14	5.028	0.090
5	4.7	22	4.744	4.6	27	4.650	0.094
6	4.3	37	4.374	4.2	34	4.268	0.106
7	3.9	45	3.990	3.8	36	3.872	0.118
8	3.6	4	3.608	3.4	42	3.484	0.124
9	3.2	10	3.220	3.0	45	3.090	0.130
10	2.8	2	2.804	2.6	35	2.670	0.134
11	2.4	20	2.440	2.3	1	2.302	0.138
12	2.0	15	2.030	1.9	45	1.890	0.140

Table 2: Variation of dark fringe width as a function of the dark fringe number towards left of the central maximum

Fringe No.	Right side of central maximum			Left side of central maximum			Fringe Width $d = d_1 \sim d_2$ (cm)
	M.S.R. (cm)	V.S.R.	Total (d_1) (cm)	M.S.R. (cm)	V.S.R.	Total (d_2) (cm)	
12	11.3	22	11.344	11.2	3	11.206	0.138
11	10.9	15	10.930	10.8	5	10.810	0.120
10	10.5	16	10.532	10.4	9	10.418	0.114
9	10.1	45	10.190	10	41	10.082	0.108
8	9.7	36	9.772	9.6	34	9.668	0.104
7	9.3	46	9.392	9.2	47	9.294	0.098
6	8.9	36	8.972	8.8	40	8.880	0.092
5	8.5	37	8.574	8.4	49	8.498	0.076
4	8.1	42	8.184	8.1	11	8.122	0.062
3	7.7	30	7.760	7.7	2	7.704	0.056
2	7.3	25	7.350	7.3	4	7.308	0.042
1	6.9	43	6.986	6.9	30	6.960	0.026

The data obtained for the variation of dark fringe width as a function of dark fringe number from the centre of the central maximum has been used to plot a graph to have a better idea of the variation. Fig. 4 depicts the variation of the dark fringe width as a function of the fringe number for a diffraction pattern obtained by a single slit. It is observed that the dark fringe width increases on both sides of the central maximum as we go away from the central maximum. It is also an indication that as we move away from the central maximum the width of the bright fringe goes on decreasing. There is a major difference between interference and diffraction patterns. The fringe width and intensity in case of interference patterns is a constant but for diffraction the fringe width varies and so does the intensity of the fringes.

It is observed that the width of the dark fringes for the Fraunhofer diffraction pattern for a single slit does not vary linearly. The increase in the dark fringe width is found to be non-linear and a fourth order polynomial function could be fitted with the experimental data points

obtained with a regression coefficient of 0.98 for both the data sets. This indicates that the intensity and the width of the bright fringes decreases much rapidly as we move away from the central maximum on both sides of the screen which follows the theory of Fraunhofer diffraction at a single slit.

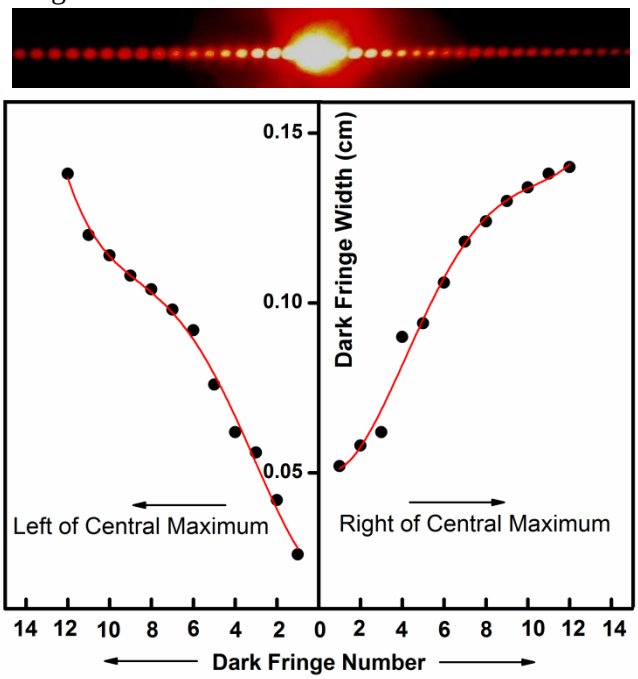

Fig. 4: Variation of dark fringe width the dark fringe numbers on both sides of the central maximum. Top of the Fig. shows the actual Diffraction pattern

3.2. Hair diameter measurement

The phenomenon of diffraction was also employed for the measurement of diameter of human hair [3]. If D is the diameter of hair, λ the wavelength of the light source used and θ is the angle of diffraction, then we have

$$D = \frac{\lambda}{\sin\theta} \quad \ldots\ldots(1)$$

The wavelength of the He-Ne laser source is known i.e., 635 nm but in order to calculate θ, the distance from the central maximum to the centre of the first dark fringe (x) along with the distance from the experimental hair to the white screen (L) was determined. The ratio of these two distances is the tangent of the diffraction angle θ as can be seen from the Fig. 5. Thus,

$$\tan\theta = \frac{x}{L} \quad \ldots\ldots(2)$$

$$\Rightarrow \theta = \tan^{-1}\left(\frac{x}{L}\right) \quad \ldots\ldots(3)$$

The data obtained for the diameter of two samples of hair collected using the above mentioned method has been tabulated in Table 3. The value of L i.e., the distance from the hair to the screen was kept fixed at 119.7 cm for the above mentioned experiment.

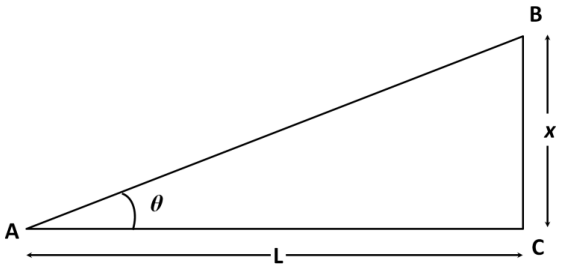

Fig. 5: Schematic diagram illustrating the method adopted for measuring of the diffracting angle

Table 3: Important Parameters for the measurement of Human Hair Diameter

Sample Name	x (cm)	θ	sin θ	D (μm)
Sample 1	0.65	0.3111	5.429×10^{-3}	116.96
Sample 2	1.00	0.478	8.353×10^{-3}	76.02

From the Table 3, it is evident that the human hair diameter obtained from the diffraction experiment for two different hair samples (Sample 1 and 2) are 116.96 μm and 76.02 μm, respectively. The average diameter of the human hair is 100 μm [4]. Thus, the results obtained by the diffraction experiment are matching with the results obtained by microscopy experiments. Hence, diffraction can be a very useful alternative for measuring hair diameter.

4. Conclusions

Fraunhofer Diffraction patterns were obtained for single, double and triangular slits employing He-Ne Laser source using a very simple experimental set-up. The variation of dark fringe width as a function of the dark fringe number has been investigated and it was observed that the fringe width in case of diffraction patterns was not constant and the dark fringe width increased non-linearly as we moved away from the central maximum. The intensity of the bright fringes thereby reduced on both sides of the central maximum which is consistent with the theory of Fraunhofer diffraction at a single slit. The measurement of human hair diameter for two different samples yielded values of 116.96 and 76.02 mm, which was found to be consistent with the average diameter of human hair measured using microscopic techniques. Diffraction thus provides a useful, low cost and reliable alternative for the measurement of human hair diameter in normal laboratories.

5. Acknowledgement

The authors would like to acknowledge the help received from Mr. Sumanta Borthakur during the

experiments. The financial assistance received under the DBT star college scheme is duly acknowledged.

6. References

[1] Optics, A. Ghatak, Tata Mc-Graw-Hill Publishers, 2005 pp 16-3.

[2] Geometrical and Physical Optics, P. K. Chakrabarti, New Central Book Agency (P) Ltd., 2004, pp 245-308.

[3] http://physicsed.buffalostate.edu/pubs/StudentIndepStudy/EURP09/Young/Young.html

[4] https://en.wikipedia.org/wiki/Hair

Bulletin of Physics Projects, 1, 2016, 29-32

Bulletin of Physics Projects

Journal homepage: http://www.bbcphysics.in/journal.html

Designing of a High Voltage DC Power Supply

Rahul Deb and Diganta Kumar Sarma[#]

Department of Physics, B. Borooah College, Ulubari, Guwahati-7, Assam, India

[#]E-mail address: sarma.diganta@gmail.com

Abstract

An assembly of three simple circuits to construct a high voltage dc power supply has been studied. The different circuits employed in the entire device are- 1) A regulated power supply, 2) A 555 timer circuit & 3) A power amplifier circuit. It has the capacity to discharge a vacuum tube and gas filled tubes. Here a flyback transformer has been used which provides a high dc voltage with saw-tooth waveform. The device is a better alternative for induction-coils used as high voltage source in discharging gas filled tubes. Apart from these the device also has the provision to work both under alternating and direct current, a part of the device can also be used as an astable multivibrator. Overall expense for the construction of the device is low and hence it is economically viable too.

1. Introduction

Charged particle accelerators have played the most crucial role in the development of nuclear physics. One of the types of particle accelerator is the electrostatic accelerator, now these require a high voltage generator or power supply. To generate high voltage was one of the first needs to pursue many scientific experiments especially in atomic and nuclear science. The oldest known types of electrostatic accelerators that are still in use are the Cockroft Walton generator and the Van de Graff generator. Over the ages the Van de Graaff generator has undergone certain changes and is now known as Pelletron. The issue with these types of generator is that safe distance is required to operate them as they have the capacity to ionize the surrounding up to a certain distance. These generators can generate voltages up to a few million volts. These two generators have been described precisely below.

1.1. Cockroft-Walton generator (Voltage multiplier):

It is a circuit comprising of a step up transformer connected to an array of diodes and capacitors. In this circuit the diodes conduct alternately and charge up the capacitor. The final voltage is taken across a line of capacitors connected in series in the multiplier circuit which serves as a number of batteries connected in series [1].

1.2. Van de Graaff generator:

It is basically a static charge accumulating device. In this device a rotating belt continuously gathers charge from a point and deposits it on a metallic dome increasing the potential of the dome and hence high voltage is obtained. These high voltage devices mostly find their applications in scientific laboratories as particle accelerators. These were the earliest methods of high voltage generation and by now these devices have undertaken many modifications. The modified version of the Van de Graaff generator is the Pelletron [2].

The primary objective of the present work is to design a high voltage generator using an assembly of timer, transistor and transformer as a substitute for induction coil to use in undergraduate laboratories for experiments where high voltage DC power supply is required.

2. Experimental Details

The methodology to generate a d.c voltage of the order of 20KV includes the use of a step down transformer along with a 555 timer, a 7812 voltage regulator, a 2N3055 transistor and a flyback transformer.

Using a step down transformer along with diodes a fully rectified power supply is made. The output is filtered using capacitors. This output is fed to a 7812 regulator for a regulated voltage. This regulated voltage is used for the 555 timer setup designed to work as an astable multivibrator. The output of the multivibrator is fed to the base of the power transistor. The emitter is grounded and the collector is positively biased through the primary of the flyback transformer. The output in the form of high voltage is obtained across the secondary of the flyback transformer. The output voltage can be regulated by regulating the frequency of the 555 timer circuit using a potentiometer in the multivibrator circuit.

2.1. The Power Supply Circuit:

The ac voltage is connected to a transformer which steps down the ac to the level for the desired dc output. A diode rectifier then provides a full wave rectified voltage which is initially filtered by a simple capacitor to produce a dc voltage. This resulting dc voltage usually has some ripple or ac voltage variation. A regulator circuit can use this dc input to provide a dc voltage that not only has much less ripple voltage, but also remains the same dc voltage even if the dc voltage varies somewhat or the load connected to the output dc voltage changes. For this voltage regulation we have taken the help of IC units. Here a 7812 IC has been used which provides a regulated voltage of 12V. The output voltage is fed to the supply terminal of the 555 timer IC. The circuit diagram of the power supply circuit depicting the use of an IC 7812 is shown in Fig. 1.

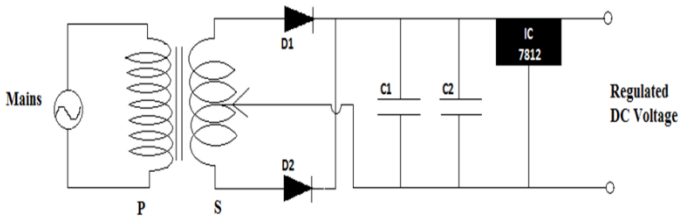

Fig. 1: Circuit diagram of Regulated Power Supply

2.2. 555 Timer as Astable Multivibrator:

The astable multivibrator generates a rectangular wave, the period of which is determined by the circuit external to IC 555. The astable multivibrator does not require any external trigger to change the state of the output, hence the name free running oscillator. The time during which the output is either high or low is determined by the two resistors and a capacitor that are externally connected to the 555 timer. The circuit diagram for the timer assembly is shown in the Fig. 2.

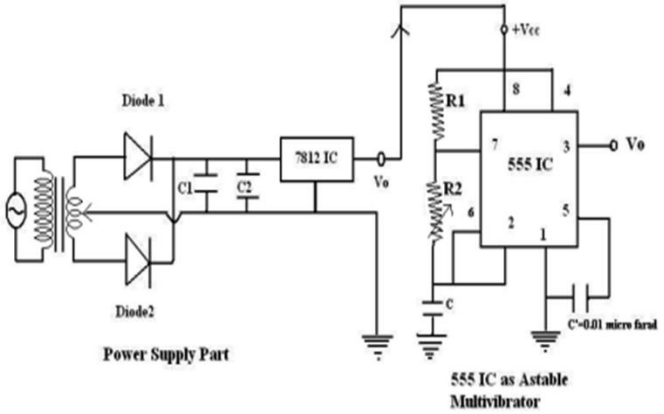

Fig. 2: Circuit diagram of the Timer Assembly

2.3. The Power Transistor:

The 2N3055 is a silicon epitaxial-base NPN transistor in Jedec TO-3 metal case [3]. It is intended for power switching circuits, series and shunt regulators, output stages and high fidelity amplifiers. The output of the timer circuit is applied to the base of the transistor through a resistor so as to stabilize the power content of the input signal of the transistor .The transistor increases the power content of the signal and apply this signal to the primary of the flyback transformer which induces the voltage and thus we obtain the high D.C voltage.

2.4. Flyback Transformer:

A flyback transformer (FBT), also called a line output transformer (LOPT), is a special type of electrical transformer. It was initially designed to generate high current sawtooth signals at a relatively high frequency. In modern applications it is used extensively in switched-mode power supplies for both low (3V) and high voltage (over 10 kV) supplies [4]. It was invented as a means of controlling the horizontal movement of the electron beam in a cathode ray tube (CRT). Unlike conventional transformers, a flyback transformer is not fed with a signal of the same wave shape as the intended output current. Unlike a power transformer which uses an alternating current of 50 or 60 Hz, a flyback transformer typically operates with switched currents at much higher frequencies in the range of 15 kHz to 50 kHz. It is a modified form of an ordinarily available step up transformer. It has a number of primaries with a single secondary. The output of this transformer is in D.C as the A.C signal is internally rectified using diodes within the

transformer. This transformer finds its use in computers and other devices having pictures tubes with high voltage requirement.

3. Results and Discussions

The device designed can generate sparks up to a length of 0.8 cm, as to generate a spark of 1cm length a voltage of nearly 30kV is required so it suggests that the voltage generated by our device is around 20kV [5]. Thus it is capable of easily discharging H_2, He, Ne, Ar filed gas tubes and has been tested in the laboratory. If the transformer used in the power supply is replaced by a transformer with higher current ratings the length of the spark developed indicates that the voltage developed is even higher. The complete circuit diagram for the high voltage power supply is shown in the Fig. 3.

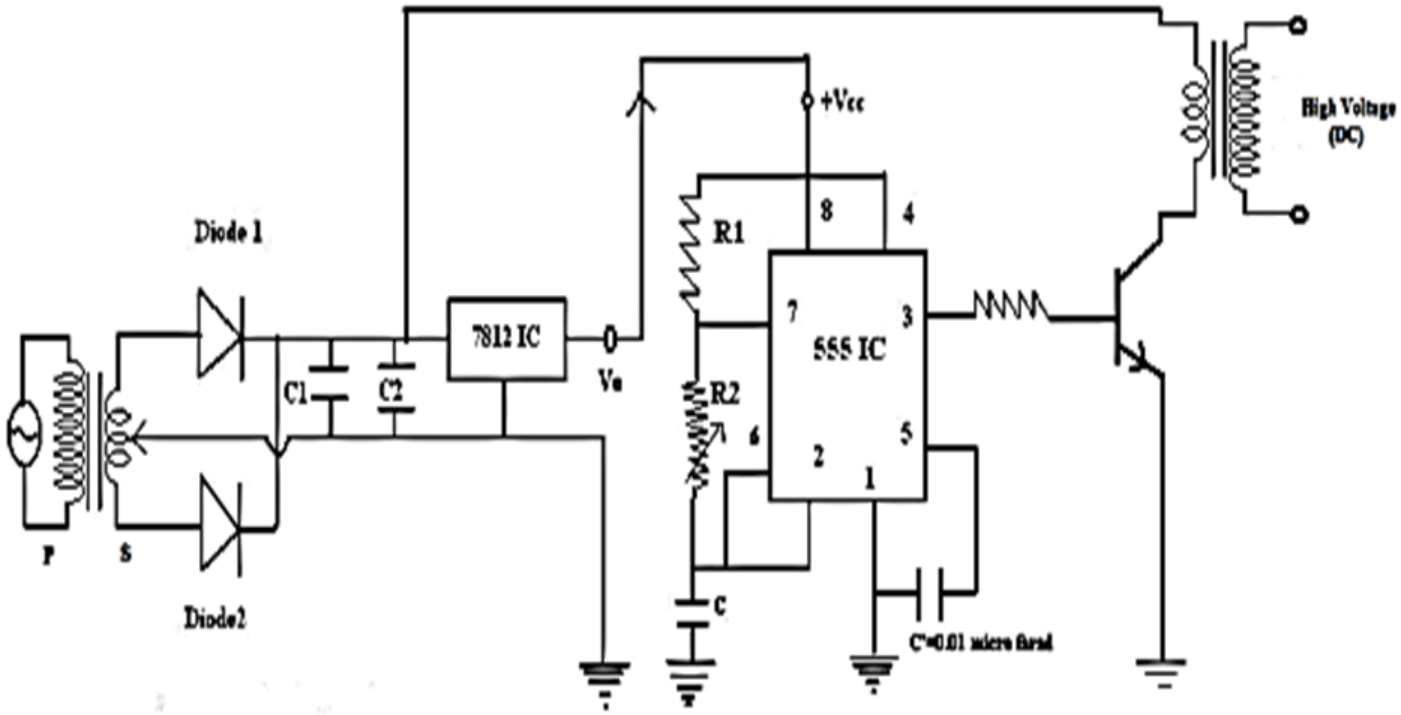

Fig. 3: Circuit diagram of the High Voltage Power Supply

3.1. The Power Amplification

The power transistor is used in the CE mode as this mode has the ability to give the maximum current and voltage amplification. This configuration is best suited for voltage, current and power gains, also the input and the output resistances of the CE mode lies between that of CB and CC mode [6]. The transistor is biased in the simplest configuration to avoid any complication that may arise due the various components used in the circuit.

3.2. Principle of operation of flyback transformer

Flyback circuits repeat a cycle of two or three stages; a charging stage, a discharging stage, and in some applications idle time following a complete discharge. Charging creates a magnetic field. The discharging action results from the collapse of the magnetic field.

Charging Stage: When the flyback transformer draws current from the power source, the current increases. This current flow creates a magnetic field flux that also increases. Energy is stored within the magnetic field. The associated positive flux change induces a voltage in the transformer which opposes the source voltage. Typically, a diode and a capacitor are series connected across the transformer winding. A load resistor is then connected across the capacitor. The diode is oriented to block current flow from the flyback transformer to the capacitor and the load resistor during the charging stage. Controlling the duty cycle the amount of energy stored during each cycle can be controlled.

Discharge Stage: The current from the source is then interrupted by opening a switch, thereby causing the magnetic field to collapse or decrease, hence a reversal in the direction of the magnetic field flux change. The negative flux change induces a voltage in the opposite direction from that induced during the charging stage. The reversed induced voltage(s) tries to create a current flow. The open switch prevents current from flowing through the power supply. With the voltage reversed, the diode now permits current flow through it, hence current flows into the capacitor and the load across the capacitor. If current can flow, then the resulting flow of current is in the

direction, which tries to maintain the existing magnetic field. The induced current cannot maintain this field but does slow down the decline of the magnetic field. A slower decline translates to a lower induced flyback voltage. If current cannot flow, the magnetic field will decline very rapidly and consequently create a much higher induced voltage. This principle, along with controlling the duration of the charging stage, allows a flyback inductor to increase or decrease the voltage without the use of a step-up or step-down turn ratio.

Idle Stage: This stage occurs whenever the flyback transformer has completely discharged its stored energy. Input and output current is at zero value.

4. Conclusions

The high voltage power supply so designed is capable of ionizing air kept at a distance of about 0.8cm. When the power supply is connected to the discharge tube it easily discharges it and when experiment is carried out with a grating a well resolved spectrum is observed. Hence it easily finds it way in a lab.

The power supply has certain advantages –

1. As the circuit itself has a frequency generator it is independent of the power source. When a dc source is used the power supply designed will be substituted by a battery or a battery eliminator.
2. The device without the final amplification and the flyback transformer serves as a frequency generator with a provision of changing the frequency also with the introduction of a variable resistor the amplitude of the wave can be varied.
3. As the voltage generated is around 20KV so the safe distance of operation of the device is very small i.e. the minimum distance that should be maintained during its operation.
4. The device so designed is simple in construction and is made from components that are easily available in the market.
5. The components used in the setup are not too expensive hence the device is economically viable too.

5. Acknowledgement

The authors should acknowledge Head of the Department for his support in finalizing the project. Special thanks to the teaching faculty of the Department for giving their valuable suggestions. Last but not the least; first author would like to thank his friends and all those people who provided me with valuable information and support for preparing this report.

6. References

[1] J. B. Gupta, “Electronic Devices and Circuits”, S. K Kataria & Sons, 2011, page 136
[2] S. N. Ghosal, “Nuclear Physics”, S. Chand & Co Ltd, 1994, page 551
[3] http:// www.sgs-thomson/microelectronics2N-3055
[4] http://www.wikipedia.org.in
[5] A. H. Howatson, "An Introduction to Gas Discharges", Pergamom Press, Oxford, 1965, page 67
[6] D. Chattopadhyay, P. C. Rakshit, “Electronics Fundamentals and Applications”, New Age International Publishers, 2008, page 168

Bulletin of Physics Projects, 1, 2016, 33-36

Bulletin of Physics Projects

Journal homepage: http://www.bbcphysics.in/journal.html

Study of Velocity Distribution of Thermionic electrons with reference to Triode Valve

Anupam Bharadwaj, Arunabh Bhattacharyya and Akhil Ch. Das[#]

Department of Physics, B. Borooah College, Ulubari, Guwahati-7, Assam, India

[#] E-mail address: akhilchdas@gmail.com

Abstract

Velocity distribution of the elements of a thermodynamic system at a given temperature is an important phenomenon. This phenomenon is studied critically by several physicists with reference to different physical systems. Most of these studies are carried on with reference to gaseous thermodynamic systems. Basically velocity distribution of gas molecules follows either Maxwell-Boltzmann or Fermi-Dirac or Bose-Einstein Statistics. At the same time thermionic emission is an important phenomenon especially in electronics. Vacuum devices in electronics are based on this phenomenon. Different devices with different techniques use this phenomenon for their working. Keeping all these in mind we decided to study the velocity distribution of the thermionic electrons emitted by the cathode of a triode valve. From our work we have found the velocity distribution of the thermionic electrons to be Maxwellian.

1. Introduction

Metals especially conductors have large number of free electrons which are basically valence electrons. Though they are called free electrons, at room temperature (around 300K) they are free only to move inside the metal with random velocities. Because, when they reach the metal surface in course of their random motion and try to leave the surface an attractive force comes into existence which prevents them from leaving the surface. Thus they have to do an amount of work against this attractive force to come out from the metal surface. The minimum energy required to do this amount of work to overcome this opposition is called work function of the metal. Work function is a temperature dependent quantity. This extra energy required by the free electrons to come out from the metal surface can be supplied by different means. One of these means is to increase the thermal energy of the free electrons by increasing the temperature of the metal. The process of electron emission by the process of increase of temperature of a metal is called thermionic emission. The amount of thermal energy given to the free electrons is used up in two ways- (i) to overcome the surface barrier and (ii) to give a velocity (kinetic energy) to the emitted electrons. The velocities so acquired by the emitted electrons vary in magnitude and direction. In our investigation we try to have an overview of the velocity distribution of the thermionic electrons.

1.1. Theory:

The free electrons in a metal move in a potential field which can be approximated as shown in the following figure. The maximum energy possessed by an electron at 0K is called Fermi energy E_F. All the energy states below E_F are filled up and all the states above it are empty. If E_0 be the height of the surface potential energy barrier then E_0- E_F is the minimum energy at 0K that enables an electron to escape from the metal. This is known as the

work function of the metal. If ϕ be the voltage equivalent of work function then-

$$e\Phi = E_0 - E_F \text{ ……………………………………} (1)$$

Obviously no electron emission is possible at 0K.

However, if temperature of metal is increased then some of electrons may be excited to higher states having energy greater than E_0 and can escape from the metal surface. Using Fermi–Dirac statistics it is possible to calculate the number of electrons which are emitted from the metal surface per sec per unit area with energies exceeding E_0 at a particular temperature of the metal (cathode). The expression for thermionic emission current density (J) is found to be-

$$J = AT^2 \exp\left(-\frac{e\Phi}{kT}\right) \text{ ……………………………} (2)$$

where, A is a constant independent of the metal, T is the temperature of the metal in Kelvin, eϕ is the work function of the metal and k is the Boltzmann constant. Above relation was first derived thermodynamically by Richardson and Dushman and is therefore known as Richardson-Dushman's equation [1].

1.2. Working Principle:

In our experiment we use a vacuum triode having concentric cylindrical electrodes- namely (i) indirectly heated cathode, (ii) grid and (iii) anode or plate as shown in the Fig. 1 and Fig. 2 [1].

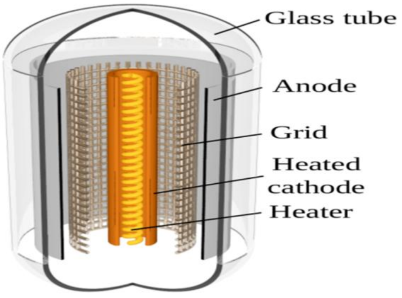

Fig. 1: Internal structure of a cylindrical triode valve

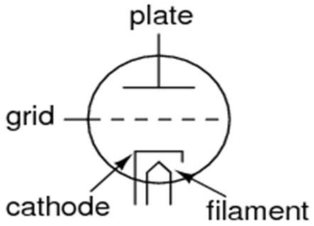

Fig. 2: Symbolic diagram of a triode valve

Using cylindrical coordinates and making a rigorous treatment it can be shown that plate current for such a triode for zero grid voltage is given by:

$$I_p = \frac{4\epsilon_0}{9}\sqrt{\frac{2e}{m}}\,\frac{2\pi L V_P^{\frac{3}{2}}}{r_p\beta^2} \text{ ………………………………} (3)$$

where L is the axial length of the electrodes, r_p is the radius of the anode and β^2 is a function of $\frac{r_p}{r_k}$ (where r_k is the radius of the cathode); its value may be taken as 1 when $\frac{r_p}{r_k}$ is large. In deriving above relation the electrons are assumed to start with zero velocity from the cathode. Eq. (3) is known as Child-Langmuir law under space charge limited condition [2].

Thus According to Child-Langmuir law the space charge limited condition the plate current I_p in a vacuum tube is related to the plate voltage V_p by the relation:

$$I_p = KV_p^{\frac{3}{2}} \text{ ……………………………………….} (4)$$

where $K = \frac{4\epsilon_0}{9}\sqrt{\frac{2e}{m}\frac{2\pi L}{r_p\beta^2}}$ is a constant for a given tube.

Now if we apply a negative grid voltage V_g, then electrons having kinetic energy less than eV_g will be obstructed by the grid from reaching the plate. As a result the plate current I_p will decrease by an amount determined by the relation:

$$\frac{1}{2}mv^2 = eV_g \text{……………………………………} (5)$$

$$v \propto \sqrt{V_g} \text{…………………………………………..} (6)$$

Thus, the velocity v of the obstructed electrons is determined by $\sqrt{V_g}$ and is determined by the decrease in plate current (I_{p0}-I_{p1}). In this way if we increase the value of negative grid voltage V_g step by step, electrons having higher and higher velocities will be obstructed and from the difference of successive plate currents we can have the number of electrons obstructed having different velocities. From these data we can draw a graph relating velocities distribution of thermionic electrons.

2. Experimental Details

The circuit arrangement for the above mentioned experiment is shown in the Fig. 3.

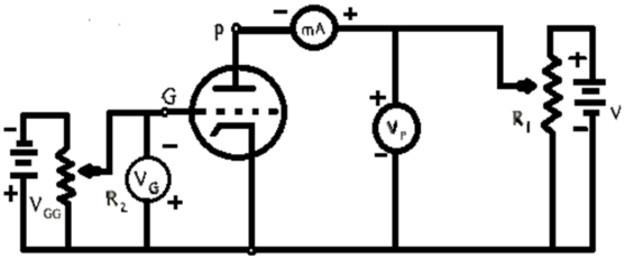

Fig. 3: Circuit diagram of the experimental set-up

3. Results and Discussions

Data were collected for the Plate Current (I_p), and difference in plate current (ΔI_p) for different grid Voltages (V_g), at constant Plate Voltage (V_p) and the process was repeated for different set of constant Plate Voltages (V_p) of 100 volts, 125 volts, 150 volts, 200 volts and 225 volts.

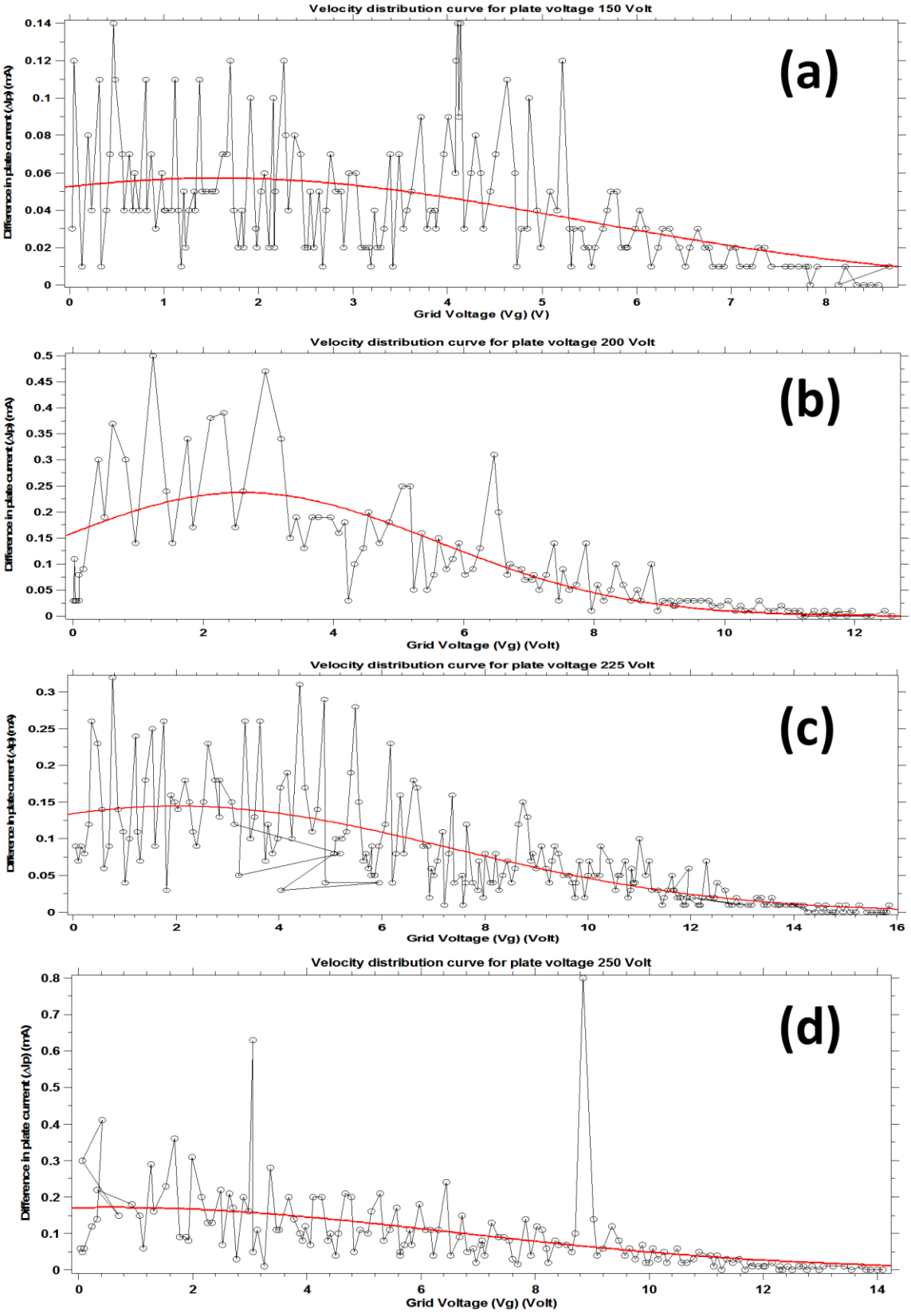

Fig 4: Variation of ΔI_p as a function of V_g for different values of plate voltages V_p (a) 150 V, (b) 200 V, (c) 225 V and (d) 250 V

The data were then plotted between the difference in plate current (ΔI_p) and grid Voltage (V_g), at a constant Plate Voltage (V_p) using MATLAB software and are shown in the Fig. 4 (a-d). Gaussian curve fitting done using MATLAB software are also shown for each plot.

4. Conclusions

From the graphs drawn using the data recorded from the above experiment the velocity distribution of the thermionic electrons of a triode valve is found to be Maxwellian. There are several picks on each graph. These picks may be attributed to various causes like (i) secondary emission of electrons due to collision of the electrons with atoms on the surface of the plate, (ii) formation of layers by the emitted electrons near the cathode and collision among the emitted electrons. Even there may be reflection effect due to the layer formation by the emitted electrons. In spite of all these effects and simplicity of the experiment the result obtained is found to be in agreement with theoretical concept regarding velocity distribution of the thermionic electrons.

5. Acknowledgement

This project was carried out as part of the Physics Major Course during 6th semester 2015 based on the new syllabus of the Gauhati University for undergraduate level under the supervision of Dr. Akhil Chandra Das, Associate Professor, Department of Physics, B Borooah College, Guwahati-781007. We express our gratitude to our respected teachers for their help during the investigation.

6. References

[1] http://www.wikipedia.com.

[2] Undergraduate level Books on electronics and statistical mechanics.

Bulletin of Physics Projects, 1, 2016, 37-40

Bulletin of Physics Projects

Journal homepage: http://www.bbcphysics.in/journal.html

Study of Optical Band Gap of Some Compounds Using Photo-Spectrometer

Chandan Choudhury, Hemanta Deka and Akhil Chandra Das[#]

Department of Physics, B. Borooah College, Ulubari, Guwahati-7, Assam, India

[#] E-mail address: akhilchdas@gmail.com

Abstract

Depending on the state of the emitting substance we can have molecular spectra for which the emitting substance must be in molecular state containing two or more atoms. Both atomic and molecular spectra are studied extensively by different scientists at different time. The search for origin of different spectral series of different elements is still going in search of the actual truth. Keeping this quest in mind we choose to explore about the optical band gap of some organic compound basically related to molecular spectra with the experimental facility available in an undergraduate level laboratory.

1. Introduction

When an absorbing medium is placed between the source and the analyzing device absorption spectrum is obtained. Depending on the distinctness of different colour bands of the spectrum may be of pure or impure nature. For experimental analysis pure spectrum is produced so that different colour bands are seen distinctly. On the other hand depending on the state of the radiating source two types spectra (i) atomic (for atomic state of the substance) and (ii) molecular (for molecular state of the substance) are obtained. When the emitting source is in atomic state (gaseous state) at very low pressure it emits line spectra. The wavelengths of different colour lines are characteristics of the element concerned. Hydrogen, Helium, etc emit this type of spectra in atomic state at very low pressure when electric discharge takes place in a discharge tube filled with these gases. When the emitting source is in molecular state at relatively higher pressure it emits band spectra. Band spectrum is sometimes called molecular spectra. For example CO_2 and N_2 gases emit this type of spectra. Optical spectroscopy can be a very useful for finding the optical band gap of compounds.

1.1. Theory:

When the emitting source is in molecular state at relatively higher pressure it emits band spectra which are called molecular spectra. Molecular spectra have different regions – (i) radio frequency region having 10 m to 1cm wavelength called nuclear magnetic resonance and electron spin resonance spectroscopy, (ii) microwave region or far infrared region having wavelength1 cm to 10^{-2} cm called rotational spectroscopy, (iii) infrared region having wavelength 10^{-2} cm to 10^{-4} cm called vibrational spectroscopy, (iv) visible and ultraviolet region having wavelength 10^{-4} cm to 10^{-8} cm called electron spectroscopy and (v) x-ray region having wave length 10^{-8} cm or less related to energy changes involving inner electrons of an atom or molecule. The internal energy of a molecule is composed of three kinds of quantized energies namely electronic, vibrational and rotational due to which a molecule can have discrete energy states. Transition between two states gives rise to spectral line in the

spectrum of that molecule. In each electronic state there are a number of possible vibrational states corresponding to different values of vibrational energy of the molecule having approximate energy difference of 0.1eV. Again each vibrational level has a set of rotational sublevel and two adjacent rotational levels in one and the same vibrational and electronic state have an energy difference of about 0.005 eV [1]. Every electronic state of a molecule has its own potential energy curve. The vertical distance between the minima of potential energy curves for lower energy state and higher energy state is equal to the difference in electronic energy of the two states. To a close approximation, the total energy E of the molecule in a given quantum state may be supposed as made up of the electronic energy E_e, the vibrational energy E_v, and the rotational energy E_r, thus

$$E = E_e + E_v + E_r \quad \text{.....(1)}$$

or in the form of energy change

$$\Delta E = \Delta E_e + \Delta E_v + \Delta E_r \quad \text{.....(2)}$$

Neglecting ΔE_v and ΔE_r which are very small in comparison to ΔE_e equation (2) can be written as:

$$\Delta E \approx \Delta E_e \quad \text{.....(3)}$$

The working of a photo spectrometer is based on the principle of electronic transition in atoms or molecules upon absorbing suitable energy from an incident light that allows electrons to exit from a lower energy state to higher excited state. When interaction with infrared light causes molecules to undergo vibrational transitions, the shorter wavelength with higher energy radiations in the UV (200-400 nm) and visible (400-700 nm) range of the electromagnetic spectrum causes many atoms or molecules to undergo electronic transitions.

When beam of light is passed through a solution the optical absorption corresponds to differences in energy states, it can be considered an indirect measure of the electronic structure. The optical band gap E_{opt} expressed in electron volts, depends on the incident photon wavelength by means of a Planck's relation:

$$E_{opt} = h\nu = \frac{hc}{\lambda} \quad \text{.....(4)}$$

where h is the Planck's constant, ν is the wave frequency and c light speed in vacuum. Experimentally, the optical band gap E_{opt} of the material is estimated by linear extrapolation from the absorption feature edge to A = 0 and subsequent conversion of the wave length (nm) into energy value versus vacuum (eV).

1.2. Optical versus electronic band-gap:

In materials with a large exciton (bound electron–hole pair) binding energy, it is possible for a photon to have just barely enough energy to create an exciton, but not enough energy to separate the electron and hole (which are electrically attracted to each other). In this situation, there is a distinction between "optical band gap" and "electrical band gap" (or "transport gap"). The optical band gap is the threshold for photons to be absorbed, while the transport gap is the threshold for creating an electron–hole pair that is not bound together. The optical band gap has lower energy than the transport gap.

In almost all inorganic semiconductors, such as silicon, gallium arsenide, etc., there is very little interaction between electrons and holes (very small exciton binding energy), and therefore the optical and electronic band gap are essentially identical, and the distinction between them is ignored. However, in some systems, including organic semiconductors, the distinction may be significant [2].

2. Experimental Details

An absorbance spectrophotometer is an instrument that measures the fraction of the incident light transmitted through a solution. In other words they are used to measure the amount of light that passes through a sample material, and by comparison to the initial intensity of light they indirectly measure the amount of light absorbed by a sample. It happens that solution of a given material will always absorb light in the same way but different amount of light having different wavelengths i.e., different colors. Some compounds absorb light other than the visible light spectrum, and that's why there are colorless solutions like water. Because different compounds absorb light at different wavelengths, thus a spectrophotometer can be used to distinguish compounds. Additionally, the amount of light absorption is directly proportional to the distance that the light traveled through a sample and the concentration of absorbing compounds in that sample. Spectrophotometers may also be used to estimate cell numbers and even identify what chemical are in a given solution. To study a compound in solution by spectrophotometry, we have to put it in a sample holder called a cuvette and place it in the spectrophotometer. Light of a particular wavelength passes through the solution inside of the cuvette and the amount of light transmitted (passed through the solution) or absorbed by the solution is recorded. To determine how much light is absorbed by the solvent and other components in the solution, we compare the absorbance of our test solution to a reference blank. We have taken potassium permanganate dissolved in water. The reference blank in this case would be water.

3. Results and Discussion

The amount of light transmitted through a solution is referred to as transmittance (*T*). The transmittance is defined as the ratio of the light energy transmitted by the

sample (I) to the energy transmitted by the reference blank (I_0).

$$T = \frac{I}{I_0} \quad \ldots\ldots(5)$$

This number is multiplied by 100 to determine the percent transmittance ($T\%$), or the percentage of light transmitted by the substance.

$$T\% = (I/I_0) \times 100 \quad \ldots\ldots(6)$$

Since the compound being tested is not present in the reference blank, the transmittance of the reference blank is defined as 100%. A certain portion of the light will be absorbed by the compound in the test cuvette, therefore the T% will be lower. For most biological applications, we measure absorbance A, (also referred to as Optical Density or OD), the amount of light that is absorbed by a solution. Absorbance is related logarithmically to transmission.

$$A = \log T = \log(I/I_0) \quad \ldots\ldots(7)$$

A=0 for the reference blank since there is no test compound present to absorb any light. Visible light is composed of wavelengths from 400 to 700 nm (nanometers). When visible light passes through a colored solution, some wavelengths are transmitted and some are absorbed and we see the colour of the transmitted wavelengths. For instance, red colour results, when a solution absorbs short wavelengths of light (green and blue) and transmits longer wavelengths (red). An absorbance spectrum (a plot of absorbance as a function of the wavelength of the incident light) is normally measured to determine the optimal wavelength (A_{max}) for measuring the absorbance of a given solution. The optimal wavelength (A_{max}) for measuring absorbance is that wavelength that is most absorbed by the compound in solution.

The light from the spectrophotometer's light source does not consist of a single wavelength, but a continuous portion of the electromagnetic spectrum. This light is separated into specific portions of the spectrum through the use of prisms or a diffraction grating. A small portion of the separated spectrum passes through a slit. When we adjust the wavelength in a spectrophotometer, we are changing the position of the prism or diffraction grating and different wavelengths of light are directed at the slit. Smaller is the slit width; better is the ability of the instrument to resolve various compounds. The small band of light coming through the slit then passes through the cuvette containing the sample. Absorbance is detected by a photocell and measured to yield the absorbance value or optical density for the sample.

The optical absorption spectra obtained for different concentrations of $KMNO_4$ and $CuSO_4$ are shown in the Fig. 1 (a, b) and Fig. 2 (a, b).

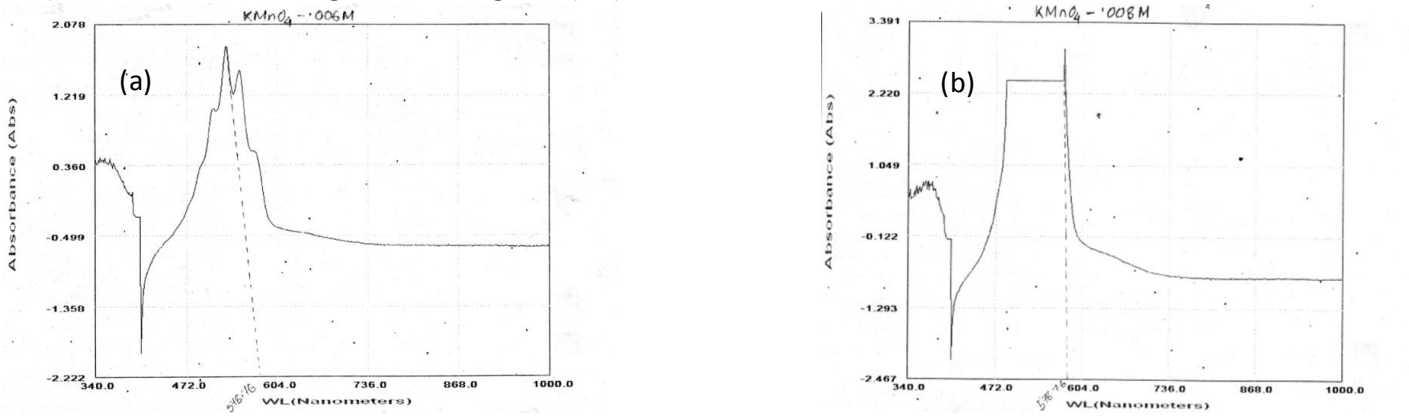

Fig. 1: Optical absorption spectra for (a) 0.006 M and (b) 0.008 M $KMNO_4$

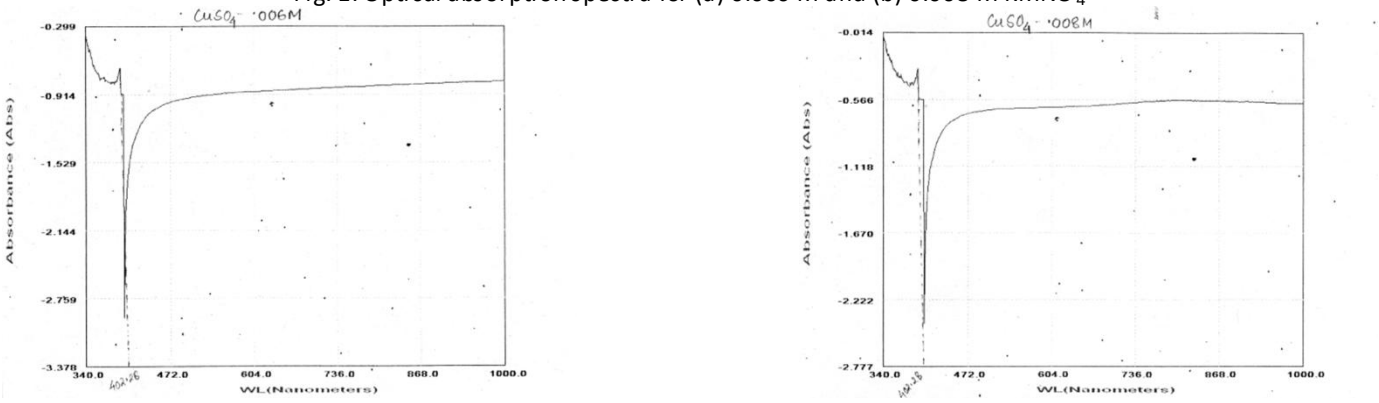

Fig. 2: Optical absorption spectra for (a) 0.006 M and (b) 0.008 M $CuSO_4$

From above results it is clear that the optical band gap is independent of concentration of the solution. The colour of a sample is determined by the absorption spectrum. When white light passes through or is reflected by a coloured substance, characteristic wavelength is absorbed. The remaining light will then assume the complementary colour to the wavelengths absorbed. Table 1 gives an idea of absorption wavelengths and the optical band gap.

Table 1: Optical band gap (eV) and Wavelength absorbed by different concentrations of different compounds

Experimental Substance	Reference substance	Serial no. of observations	Concentration of the experimental substance (M)	Wavelength corresponding to maximum absorption (nm)	Optical band gap (eV)
$KMNO_4$	Water	1	0.006	578.76	2.1
		2	0.008	578.76	2.1
		1	0.006	402.28	3.0
$CuSO_4$	Water	2	0.008	402.28	3.0
		3	0.01	402.28	3.0

4. Conclusions

In the present work we have investigated the optical absorption spectra of some selected chemical compounds with the aim of determining their optical band gap. It was observed that the optical band gap of a particular compound is not affected by the concentration of the sample in solution. Thus the optical band gap is fixed for a compound.

5. Acknowledgements

We would like to acknowledge the help and assistance received from the faculty members of our department during the course of this work.

6. References

[1] http://www.wikipedia.com.

[2] Fundamentals of Molecular Spectroscopy, Banwell and McCash, McGraw Hill Education (India).

Bulletin of Physics Projects

Journal homepage: http://www.bbcphysics.in/journal.html

Study of Rain Drop Size Distribution with the help of Disdrometer observation

Pranab Dutta, Diganta Kumar Sarma[#]

Department of Physics, B. Borooah College, Ulubari, Guwahati- 781007, Assam

[#] E-mail address: sarma.diganta@gmail.com

Abstract

The paper deals with the study of Rain Drop Size Distribution (DSD) with rain rate as observed from the Disdrometer data at North Eastern Space Application Centre, Shillong. It was observed that rain in this station consists of drops with various diameter ranging from 0.3 mm to ~4 mm. Drops with diameter ranging between 1.5 mm to 3 mm were observed to be have maximum occurrences. Rain rate was calculated from the observed DSD. The rain DSD were observed for different rain rate categories viz. low, moderate and high. The DSD pattern observed for these categories are found to be different. For low rain rate drops with diameter ~ 1 mm have maximum contribution, whereas for high rain rate drop diameters between 2 to 3 mm have maximum contribution.

1. Introduction

Due to the absorption of solar energy by earth, evaporation occurs when the atmosphere becomes unstable and support convection, the water vapour rises vertically upward and reaches cooler region of atmosphere. As a result it is no longer possible for the air to hold it in vapour form and it starts condensing to form liquid droplets which are known as cloud. Eventually when cloud droplets grew and become large enough to fall we get rain. Two mechanisms have been proposed for formation of rain: Bergeron process Collision-coalescence process. Bergeron process is related to the formation of precipitation to super cooled (below 0^0C) clouds.

Collision-coalescence process is related to the formation of precipitation in warm clouds (above 0^0) in which large cloud droplets collide and join together (coalescence) to form rain drops. Especially in tropic region precipitation is mainly due to collision–coalescence process. Figure below shows how rain is formed by the mechanism of collision– coalescence process. When an initially spherical droplet falls, it flattens out into a pancake shape. As it gets wider and thinner it eventually captures the air in front of it to form the shape of an upturned bag. Finally, as the bag inflates to a certain size it breaks apart into many smaller droplets- droplets whose size distribution mimics that of natural rainfall.

Rain Drop Size Distribution (DSD) is one of the most fundamental rain parameter to study and characterize different precipitating systems. The study of DSD is of two folds. On one hand it contributes to a better understanding of microphysical and cloud processes in the generation of precipitation particles [1-3] and the other hand it

contributes to the remote measurements of precipitation by radars and satellites [4-6].

This project work is based on the basic observations of rain drop sizes with an instrument called Disdrometer located at a center North Eastern Space Application Center (NESAC), Shillong under Department of Space.

The main objectives of this work are to study the working of the disdrometer in details, analyze the sizes of rain drops and subsequently the drop size distribution as observed by disdrometer and to calculate rain rate from the observed rain drop size distribution. Another important feature of the present work is to investigate the variation of drop sizes for different rain rates.

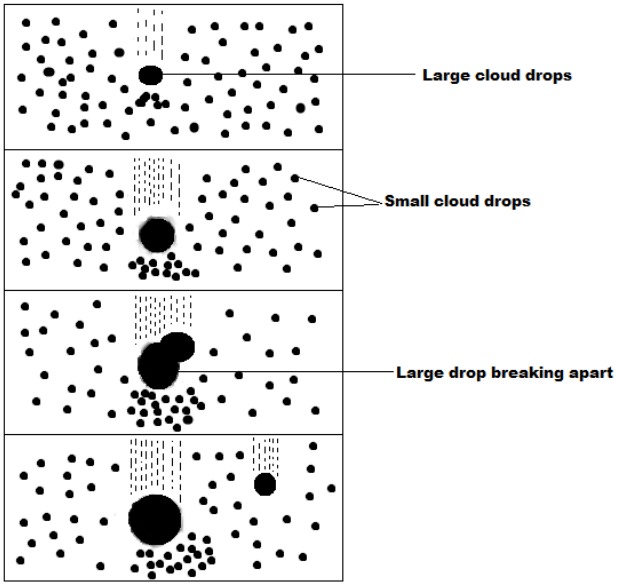

Figure 1: Rain formation mechanism by collision– coalescence process

2. System description and Data analysis:

2.1. Disdrometer specifications:

The Joss-Waldvodgel disdrometer (RD-80) is an instrument for measuring raindrop size distribution continuously and automatically. Basically the disdrometer estimates the diameter of rain drops.

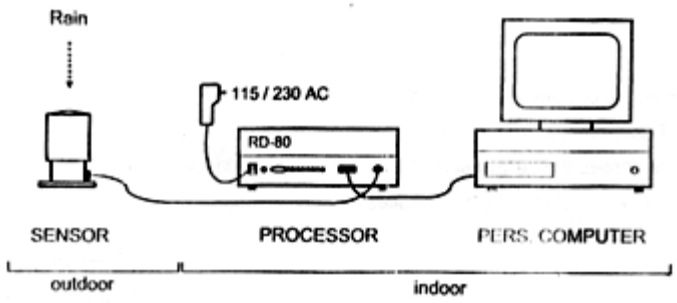

Figure 2: Schematic diagram of the Disdrometer.

The instrument transforms the vertical momentum of an impacting raindrop into an electric pulse whose amplitude is a function of the drop diameter. A conventional pulse height analysis yields the size distribution of the raindrops. The RD-80 disdrometer for raindrops consists of three units: (i) the sensor which is exposed to rain, (ii) The processor (iii) A plug in power supply for powering the processor. The sensor transforms the mechanical momentum of an impacting drop into an electrical pulse. The amplitude of the pulse is roughly proportional to the mechanical momentum. The sensor consists of a cylindrical metal housing, containing an electromechanical transducer and an amplifier module. The processor contains circuit to eliminate unwanted signals, mainly due to acoustic noise and produces a 7 bit code at the output for every drop, hitting the sensitive surface of the sensor. The specifications of the Disdrometer are listed in Table 1.

Table 1: Specifications of the disdrometer

Disdrometer parameters	Specifications
Range of drop diameter	0.3 mm to 5mm
Sampling area	50 cm^2
Accuracy	± 5% of measured drop diameter
Channels	20 classes distributed more or less exponentially over the range of drop diameters.
Power requirements	Plug in power supply included in delivery: 115/230 Volts AC, 5.5 VA, 50/60 Hz
Operating temperature range	0 to 4 degree Celsius for processor 0 to 50 degree Celsius for sensor
Dimensions of the sensor	10cm x 10cm x 17cm sensor
Dimensions of processor	12cm x 26cm x 27cm deep
Weight	Sensor: 2.9 kg; Processor: 2.2 kg
Standard length of sensor cable	20 m

2.2 Recording of data:

To operate the system the following procedures are followed.

i. Connect the sensor to the processor.
ii. Connect the processor to a free and usable serial input (COM 1 to COM 4) of the PC using the standard 9 pin D-sub cable.
iii. Connect the plug-in-power supply to the processor DC power connection
iv. Turn on power of the processor and of the PC.
v. Then start the program.

Disdrometer detects sizes of various rain drops in 20 channels ranging from 0.313 to 5.101 mm. From each channel the number of drops accumulated can be known.

Table 2: Rain rate calculated for different time

Date	Time	Diameter in mm																				Rain Rate in mm/h
		0.35	0.45	0.55	0.65	0.77	0.91	1.11	1.33	1.51	1.66	1.91	2.26	2.58	2.86	3.19	3.54	3.91	4.35	4.85	5.37	
7/2/2009	**6:14:00**	0	0	5	10	22	65	169	163	120	129	192	142	70	28	16	2	2	2	0	0	**46.7**
7/2/2009	**6:15:00**	0	4	22	32	44	93	183	197	130	133	226	115	26	6	2	0	0	0	0	0	**34.19**
7/2/2009	**6:16:00**	0	0	12	19	32	69	182	177	141	134	206	130	49	11	7	1	1	0	0	0	**39.1**
7/2/2009	**6:17:00**	1	4	11	45	46	82	171	138	99	115	203	99	27	5	2	0	0	0	0	0	**29.78**
7/2/2009	**6:18:00**	2	11	42	73	57	92	165	156	101	126	138	34	12	2	1	0	0	0	0	0	**20.69**
7/2/2009	**6:19:00**	1	7	15	35	33	70	131	123	92	103	121	71	27	10	4	0	0	0	0	0	**24.13**
7/2/2009	**6:20:00**	0	0	4	14	30	67	102	112	82	91	159	98	55	26	16	3	3	0	0	0	**36.55**
7/2/2009	**6:21:00**	0	1	20	36	38	60	135	134	80	108	140	72	27	11	2	0	0	0	0	0	**24.83**
7/2/2009	**6:22:00**	3	15	42	42	46	65	168	127	96	87	145	35	4	0	0	0	0	0	0	0	**17.84**
7/2/2009	**6:23:00**	4	28	54	52	45	78	170	111	94	91	70	15	0	0	0	0	0	0	0	0	**12.62**
7/2/2009	**6:24:00**	15	52	59	73	52	52	146	167	81	39	39	9	0	0	0	0	0	0	0	0	**9.608**
7/2/2009	**6:25:00**	2	33	44	46	41	69	193	154	65	67	72	23	3	1	0	0	0	0	0	0	**13.2**
7/2/2009	**6:26:00**	13	35	53	60	36	82	200	126	74	48	45	3	3	0	0	0	0	0	0	0	**9.795**
7/2/2009	**6:27:00**	9	30	31	66	69	79	173	150	62	62	59	17	1	1	0	0	0	0	0	0	**11.69**
7/2/2009	**6:28:00**	5	31	45	75	64	75	185	161	77	46	61	11	1	0	0	0	0	0	0	0	**11.31**
7/2/2009	**6:29:00**	5	29	43	57	47	69	187	133	47	44	36	11	2	0	0	0	0	0	0	0	**9.113**
7/2/2009	**6:30:00**	11	33	52	62	57	55	101	67	41	38	41	10	3	1	0	0	0	0	0	0	**7.47**

The average diameter of the 20 channels are 0.359 mm, 0.455 mm, 0.551 mm, 0.656 mm, 0.771 mm, 0.913 mm, 1.116 mm, 1.331 mm, 1.506 mm, 1.665 mm, 1.912 mm, 2.259 mm, 2.584 mm, 2.869 mm, 3.198 mm, 3.544 mm, 3.916 mm, 4.350 mm, 4.859 mm and 5.373 mm.

3. Results and Discussions

3.1. Rain drop sizes observed by disdrometer:

The disdrometer data on 1st & 2nd July 2009 were collected from NESAC. Figure 3 shows the distribution of rain drops of various diameters for the 2nd July event.It can be observed that the occurrences of number of drops having diameter ranging between 1.5 mm to 3 mm are maximum while the low and high diameter drops are less. Particularly for the time about 0300 IST to 0500 IST two peaks can be seen from the figure. This is the period where rain rate was very high. High rain rate consists of rain drops of larger diameter. The figure also depicts the existence of larger diameter of about 2-3 mm. This shows the rain consists of various sizes drops with contribution of middle ranges diameter are maximum. From the figure two peaks can be observed. This may be attributed to collision and coalescence process. Because of collision bigger drops breaks into small drops and because of coalescence smaller drops turns into bigger drops.

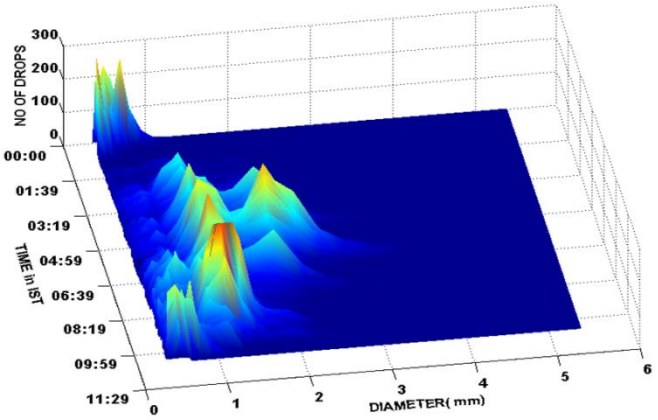

Figure 3: Number of rain drops of various diameters with time.

3.2. Measurement of rain from disdrometer data:

Disdrometer detects sizes of various rain drops in 20 channels ranging from 0.313 to 5.101 mm. from each channel the number of drops accumulated can be known. Using the rain rate equation below the rain fall rate can be calculated.

$$R = \frac{\pi}{6} \times \frac{3.6}{10^3} \times \frac{1}{AT} \times \sum n_i D_i^3$$

where, n_i = number of drops in a the channels

D_i = diameter of the drops.

A = area of the sensitive surface of the disdrometer (50 cm^2)

T = time interval (60 sec)

Table 2 shows some sample data with number of drops of different diameter (channels) with the corresponding rain rates. From the table it can be noticed that for high rain rate number drops in the higher diameter ranges are more as can be noticed for the time 06:14 IST on 02 July 2009 data (Table 2). Whereas for the low rain rate number of drops decreases as can be inferred for the time 06:40 IST (last row of Table 2).

3.3 Variation of DSD for different rain rates:

From the collected data we have categorized rain rate into three classes as low, medium and high. For the present study the ranges of rain rate considered are (a) Low rain (0<R<10 mmh^{-1}), (b) Medium rain (10<R<30 mmh^{-1}) and (c) High rain (30<R mmh^{-1}).

It can clearly be noticed from the Figure 4 that for low rain rate number of rain drops of lower diameter (~1 mm) are maximum while for medium and high rain rates larger diameter (~2-3 mm) are maximum.

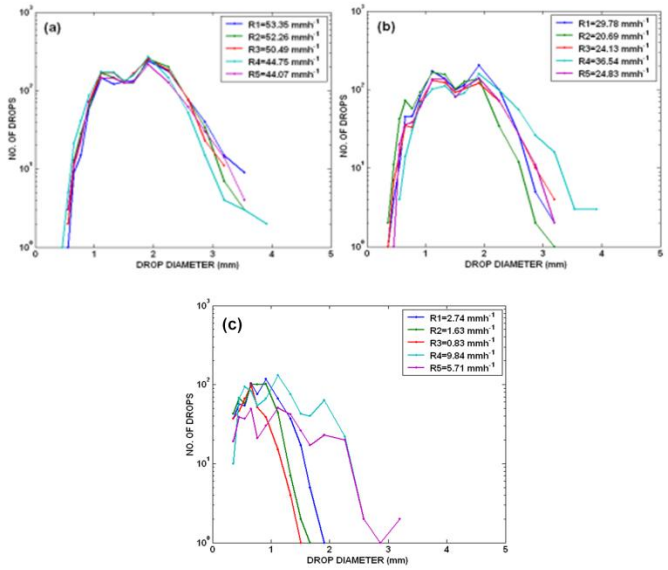

Figure 5: Variation of rain drop sizes for (a) Low rain (0<R<10 mmh^{-1}), (b) Medium rain (10<R<30 mmh^{-1}) and (c) High rain (30<R mmh^{-1}) rates.

4. Conclusions

A preliminary study has been conducted on rain drop sizes and rain rate over Shillong. An instrument called Disdrometer which is located at NESAC, Shillong, gives the sizes of various rain drops. This work explores the working of disdrometer for observation of diameter of various rain drop sizes and subsequently the measurement of rain from the observed data.

The main conclusions of this study are:

(a) Rain consists of various drops of different sizes ranging from 0.3 mm to 4 mm.

(b) In this region of study it is observed that rain rate is mainly contributed by medium sizes rain drops.
(c) For low rain rate larger drops are not observed while for high rain rate drop sizes of the order of about 4 mm is observed.

5. Acknowledgement

The authors would like to thank the Director, NESAC for allowing us to visit the station and using the Disdrometer data. Authors would like to acknowledge Dr. Arup Borgohain and Mr. Shyam Sundar Kundu from NESAC for their valuable suggestions and help during the work.

6. References

[1] Gossard, E. E., Measuring drop size distributions in cloud with a clear-air sensing Doppler radar, J. Atmos. Oceanic Technol., 5, 640 – 649, 1988.

[2] Tokay, A., and D. A. Short, 1996: Evidence from tropical raindrop spectra of the origin of rain from stratiform versus convective clouds. J. Appl. Meteor., 35, 355–371.

[3] Mahen Konwar, Diganta Kumar Sarma, Jyotirmoy Das and Sanjay Sharma, 2006, Shape of the rain drop size distributions and classification of rain type at Gadanki *Indian Journal of Radio and Space Physics*, Vol. 35, pp. 360-367.

[4] Richard J. Doviak, 1983: A Survey of Radar Rain Measurement Techniques. *J. Climate Appl. Meteor.*, 22, 832–849.

[5] Atlas D., R. S. Srivastava, R. S. Sekhon 1973, Doppler radar characteristics of precipitation at vertical incidence , *Rev. Geophys. Space Phys*. Vol. 11, pp. 1-35.

[6] Sarma D. K., M. Konwar, S. Sharma, S. Pal, J. Das, U. K. De, G. Viswanathan, 2008, An Artificial Neural Network based integrated regional model for rain retrieval over land and ocean, *IEEE. Trans. Geosci. Remote Sens.* Vol. 46, pp.1689-1696